Title
ELECTRONIC ENERGY LEVELS OF THE f ELECTRON ELEMENTS

Author
Conway, John G.

Publication Date
1965

UCRL-10872

University of California

Ernest O. Lawrence
Radiation Laboratory

HYPERFINE STRUCTURE SEPARATION, NUCLEAR MAGNETIC MOMENT, AND HYPERFINE STRUCTURE ANOMALY OF CESIUM-131

Berkeley, California

DISCLAIMER

Research and Development

UCRL-10872
UC-34 Physics
TID-4500 (19th Ed.)

UNIVERSITY OF CALIFORNIA

Lawrence Radiation Laboratory
Berkeley, California

Contract No. W-7405-eng-48

HYPERFINE STRUCTURE SEPARATION, NUCLEAR MAGNETIC MOMENT, AND HYPERFINE STRUCTURE ANOMALY OF CESIUM-131

Richard D. Worley

(Thesis)

June 13, 1963

Printed in USA. Price $2.00. Available from the
Office of Technical Services
U. S. Department of Commerce
Washington 25, D.C.

HYPERFINE STRUCTURE SEPARATION, NUCLEAR MAGNETIC MOMENT, AND HYPERFINE STRUCTURE ANOMALY OF CESIUM-131

Contents

HYPERFINE STRUCTURE SEPARATION, NUCLEAR MAGNETIC MOMENT, AND HYPERFINE STRUCTURE ANOMALY OF CESIUM-131

Richard D. Worley

Lawrence Radiation Laboratory and Department of Physics
University of California
Berkeley, California

June 13, 1963

ABSTRACT

The atomic-beam magnetic-resonance method was used to obtain the hyperfine structure separation $\Delta\nu$, the nuclear magnetic dipole moment μ_I, and the hyperfine structure anomaly Δ, of Cs^{131}. Independent values of μ_I and $\Delta\nu$ were obtained by observing one of the $\Delta F = \pm 1$ doublets in a field-independent region. The measurements were made for the $^2S_{1/2}$ electronic ground state; the values obtained are

$$\Delta\nu = 13181.3805\ (30)\ \text{Mc/sec},$$

$$\mu_I = 3.525\,(4)\ \text{nm},$$

$$g_I = 7.678\,(8)\times 10^{-4},$$

$$^{131}\Delta^{133} = -0.65\,(10)\,\%,$$

$$^{131}\Delta^{135} = -0.61\,(10)\,\%.$$

The values of μ_I and g_I are not corrected for diamagnetic shielding. A theoretical nuclear magnetic moment was calculated by using configuration mixing theory (CMT). The above anomalies were compared with the Bohr-Weisskopf theory and the CMT. Experimental values of the anomalies agree with the predicted values to within the estimated errors, and the ground-state configuration of Cs^{131} appears to be a mixture of $2d_{5/2}(1g_{7/2})^4$ and $(1g_{7/2})^2(2d_{5/2})^3$ configurations.

I. INTRODUCTION

The structure of the nucleus has been a subject of interest since about 1910. Following 1930 and the development of high-energy particle accelerators, the nucleus could be broken apart and studied in terms of nuclear forces, in hopes of explaining nuclear structure. Another approach to the understanding of nuclear structure is by viewing the interaction of the nucleus not only with its electrons but also with any environment external to the atom, as with a magnetic field. In this case, the nucleus is considered an entity on an equal basis with the cloud of electrons about it and each coupled to the other. It is the coupled quantity that interacts with the forces external to the atom. Information about the interaction yields information about the nucleus. The existing theories of the nucleus are used to interpret this information in terms of nuclear structure. An experiment using this latter approach is the subject of this paper.

The atomic-beam method introduced by Rabi (RAB 38) is a very appropriate method for the study of the above interaction. There are no nearest-neighbor interactions to contend with and at high vacuums there are relatively few collisions. Thus the method itself does not introduce any further complications to the interpretation of the interaction.

The nuclear entity manifests itself in the work considered here through a nuclear magnetic moment $\underset{\sim}{\mu}_I$ and a spin $\underset{\sim}{I}$. These quantities are considered on an equal basis as the electronic magnetic moment $\underset{\sim}{\mu}_J$ and angular momentum $\underset{\sim}{J}$; each of these quantities is coupled to the other and each interacts with an external magnetic field $\underset{\sim}{H}$. For the interpretation of nuclear structure two important effects are considered. First, the nuclear moment μ_I will be measured and compared with its theoretical counterpart. The theoretical value of μ_I may be arrived at by viewing the nucleus as composed of neutrons and protons all coupled together, and therefore the measured value of μ_I will clarify the coupling problem somewhat. The second effect comes about by considering the interaction of μ_I and μ_J alone; i.e., with no external

field. For example, the electrons may be considered to interact with a point nucleus. If, however, as in the case of cesium, there exists an unpaired $S_{1/2}$ electron, then—since its wave function is nonzero at the nucleus—it will penetrate within the volume of the nucleus. The interaction of the electron with the distribution of volume magnetization due to the nucleons as compared with the interaction of the electron with a point nucleus is referred to as the hyperfine structure (hfs) anomaly. The hfs anomaly also depends on the coupling of the nucleons and therefore represents another independent test for the theories of nuclear structure.

Isotopes of an element are different from one another in that each one has a different number of neutrons from the others. They have the same nuclear charge and their charge distributions should be quite similar. The nucleon coupling will vary perhaps as neutrons are added and it is instructive to investigate this variation. The hfs anomaly can be calculated for two isotopes and their difference can be a measure of the change of coupling. Such experiments have been performed for Cs^{133} and Cs^{135} and the results have been reported by Walchli (WAL 53) and by Stroke, Jaccarino, Edmonds, and Weiss (STR 57), respectively. The present experiment is for Cs^{131}, and the anomaly between these three isotopes may be evaluated and compared with theory. Nuclear structure inference may then be made for these isotopes.

This thesis is meant to be complete, yet in places will be very concise and information will be referenced. For example, the hyperfine interaction has been adequately discussed in a number of texts but the hfs anomaly has not. Therefore, Sec. III has commanded more attention than Sec. II, concerning details and derivations. Section IV is a detailed account of the procedure used in the experiment. Considerable difficulty was met when high radio frequencies were used in the experiment. Two results followed. First, a second atomic-beam machine had to be used to finish the experiment and, second, a considerable time was spent analyzing the data (resonances). Thus,

Sec. V describes both machines, and under experimental results there is a careful analysis of the high-frequency data. In Sec. VI the nucleon coupling is arrived at by using the CMT as applied to the calculation of nuclear moments and anomalies.

II. THEORY OF THE HYPERFINE STRUCTURE INTERACTION

As is briefly discussed in the introduction, this experiment measures the interaction between the nuclear magnetic moment $\underset{\sim}{\mu}_I$, the atomic magnetic moment $\underset{\sim}{\mu}_J$, and an externally applied magnetic field $\underset{\sim}{H}_0$. The interaction between atoms is neglected since in an atomic beam the distance between them is large.

If there is no externally applied magnetic field, the $\underset{\sim}{\mu}_I$ and $\underset{\sim}{\mu}_J$ interact to produce an energy $h\Delta\nu$ between adjacent energy levels, where h is Planck's constant (erg-sec) and $\Delta\nu$ is measured in cycles per second. The quantity $h\Delta\nu$ is called the hfs splitting. Thus, in the case of the cesium atom the atomic ground-state energy is split into two levels separated by $h\Delta\nu$. Each magnetic dipole moment generates a magnetic field in which the other is located, and it is this interaction that gives rise to the splitting. The behavior of the dipole in the magnetic field is to precess about the direction of the field. Since $|\underset{\sim}{\mu}_J|$ is approximately 2000 times as strong as $|\underset{\sim}{\mu}_I|$, $\underset{\sim}{\mu}_I$ will precess about the magnetic field produced by the electrons. The energy of separation is usually written

$$\Delta W = h\Delta\nu = \frac{ha}{2}(2I + 1), \qquad \text{(II. 1)}$$

where I is the nuclear spin. This relationship is also taken as the definition of "a" measured in cycles per second; "a" is referred to as the hfs constant.

With the application of an external inhomogeneous magnetic field, the forces on an atom are represented by

$$\frac{\partial W}{\partial X} = -\frac{\partial W}{\partial H}\frac{\partial H}{\partial X} \equiv \mu_{eff}\frac{\partial H}{\partial X}, \qquad \text{(II. 2)}$$

where X is the dimension along the beam. And if the quantity μ_{eff} is nonzero, the atom will be deflected in the direction of the gradient of the field, which is usually at right angles to the beam. This is a prime consideration in the operation of an atomic-beam machine.

Once the gradient is established, the sign of μ_{eff} determines whether the deflection is parallel or antiparallel to the gradient.

The application of a homogeneous field will produce no deflection, and the only effect will be to remove the degeneracies in the wave function at zero field and give rise to separated energy levels. The separation of these levels depends on whether the field is weak, strong, or intermediate. By a weak field it is meant that the applied field is too small to decouple the nucleus from the cloud of electrons. A strong field is one for which $\underset{\sim}{\mu}_I$ and $\underset{\sim}{\mu}_J$ are decoupled and independently precessing about the applied field. The calculation of the three cases will now be indicated; for further details the reader is referred to any good text on atomic or molecular beams, such as (RAM 56).

The Hamiltonian may be shown to be

$$\mathcal{H} = ha\, \underset{\sim}{I} \cdot \underset{\sim}{J} - g_I \mu_0\, \underset{\sim}{I} \cdot \underset{\sim}{H}_0 - g_J \mu_0\, \underset{\sim}{J} \cdot \underset{\sim}{H}_0 , \qquad \text{(II. 3)}$$

where H_0 is the homogeneous applied magnetic field; $\underset{\sim}{I}$ and $\underset{\sim}{J}$ are the nuclear and atomic spins, respectively; μ_0 is the Bohr magneton measured in ergs per gauss, and the values of g_I and g_J are given by

$$\underset{\sim}{\mu}_I = \mu_0 g_I \underset{\sim}{I} , \quad \underset{\sim}{\mu}_J = \mu_0 g_J \underset{\sim}{J}, \qquad \text{(II.4)}$$

and where I and J are good quantum numbers. Different cases depending on the strength of H_0 are considered next.

A. Low-Field Interaction

For small applied fields the dominant term is the first term; the other two are considered perturbations. In this case $\underset{\sim}{I}$ and $\underset{\sim}{J}$ are tightly coupled to produce a resultant $\underset{\sim}{F}$,

$$\underset{\sim}{F} = \underset{\sim}{I} + \underset{\sim}{J}, \qquad \text{(II. 5)}$$

and it is $\underset{\sim}{F}$ that couples to the external field $\underset{\sim}{H}_0$, giving the projections m_F, defined by

$$\underset{\sim}{F} \cdot \underset{\sim}{H}_0 = m_F H_0. \qquad \text{(II. 6)}$$

There are $2F+1$ of these projections. The energy levels are given by

$$W(F, m_F) = \frac{ha}{2}[F(F+1) - I(I+1) - J(J+1)] - g_J[F(F+1) + J(J+1) - I(I+1)]$$

$$\frac{\mu_0 H_0}{2F(F+1)} m_F - g_I[F(F+1) + I(I+1) - J(J+1)] \frac{\mu_0 H_0}{2F(F+1)} m_F. \qquad \text{(II.7)}$$

As will be clear later the quantity of interest is the transition frequency between two energy levels. The particular transitions for which $\Delta m_F = \pm 1$ are called π transitions; these were used throughout the experiment. The σ transitions are those for which $\Delta m_F = 0$. For $\Delta F = 0$, $\Delta m_F = \pm 1$, the frequency becomes

$$\nu_0 \approx \frac{g_J \mu_0}{2I+1} \frac{H}{h} , \qquad \text{(II.8)}$$

where H is measured in gauss and ν_0 in cycles per second. In deriving this relationship, g_I was neglected in relation to g_J from the same argument used above pertaining to the relative moments. Also, for the case at hand the only possibilities for F are $F=I\pm 1/2$, since the atomic state of cesium is $^2S_{1/2}$. For $\Delta F=\pm 1$, $\Delta m_F=\pm 1$, the frequency is approximately $\Delta\nu$; both of these π transitions will be used in the measurement of $\Delta\nu$.

B. High-Field Interaction

For the high-field limit the energy levels are given by

$$W(m_I, m_J) = ham_I m_J - g_J \mu_0 m_J H_0 - g_I \mu_0 m_I H_0, \qquad \text{(II.9)}$$

where it is recalled that for this case $\underset{\sim}{\mu}_I$ and $\underset{\sim}{\mu}_J$ precess independently about H_0, resulting in the projections $\underset{\sim}{I} \cdot \underset{\sim}{H}_0 = m_I H_0$ and $\underset{\sim}{J} \cdot \underset{\sim}{H}_0 = m_J H_0$. Transitions between these levels are not used in the experiment. These transitions would have to be made at magnetic fields of about 10^4G.

C. Intermediate-Field Interaction

Here H_0 is of intermediate strength and the calculation of the splitting is not so straightforward as the other two cases; but, however, it is a very important region for the experiment. Reference is given to Ramsey (RAM 56) for the calculation; the results for $J = 1/2$ are stated below. The following solution is known as the Breit-Rabi equation, and its pictorial representation the Breit-Rabi diagram:

$$W(F, m_F) = \frac{-h\Delta\nu}{2(2I+1)} - g_I \mu_0 H_0 m_F \pm \frac{h\Delta\nu}{2}\left(1 + \frac{4m_F X}{2I+1} + X^2\right)^{1/2}, \quad \text{(II. 10)}$$

where $X = (g_I - g_J)\,\mu_0 H_0 / h\Delta\nu$.

The positive sign is used for the state $F = I + 1/2$, and the negative sign for the state $F = I - 1/2$. By using the values of the constants in the Appendix, $W(F, m_F)$ is plotted for Cs^{131} in Fig. 1. The transitions between levels 1 and 2 are

$$\nu_{12} = -\frac{g_I \mu_0 H_0}{h}(m_1 - m_2) + \frac{\Delta\nu}{2}\left[(\pm)_1\left(1 + \frac{4m_1}{2I+1}X + X^2\right)^{1/2} - (\pm)_2\left(1 + \frac{4m_2}{2I+1}X + X^2\right)^{1/2}\right] \quad \text{(II. 11)}$$

Here $(\pm)_1 = (\pm)_2$ if m_1 and m_2 belong to same F level, and $(\pm)_1 = -(\pm)_2$ if m_1 and m_2 belong to different F levels. This result can be shown to reduce to each of the other two cases in the proper limit of H_0. For example, by expanding the square root in terms of H_0, an expression corresponding to Eq. (II. 8) with slightly more accuracy can be obtained for the low-field case $\Delta F = 0$, $\Delta m_F = \pm 1$,

$$\nu \approx \nu_0 + \nu_0^2 \frac{2I}{\Delta\nu} , \quad \text{(II. 12)}$$

where all definitions and units are the same as Eq. (II. 8). This will be the more useful approximate relationship in discussing the experiment.

Another important application of (II. 11) is for the case of the doublet $\Delta F = \pm 1$ and $\Delta m_F = \pm 1$ occurring at a particular magnetic

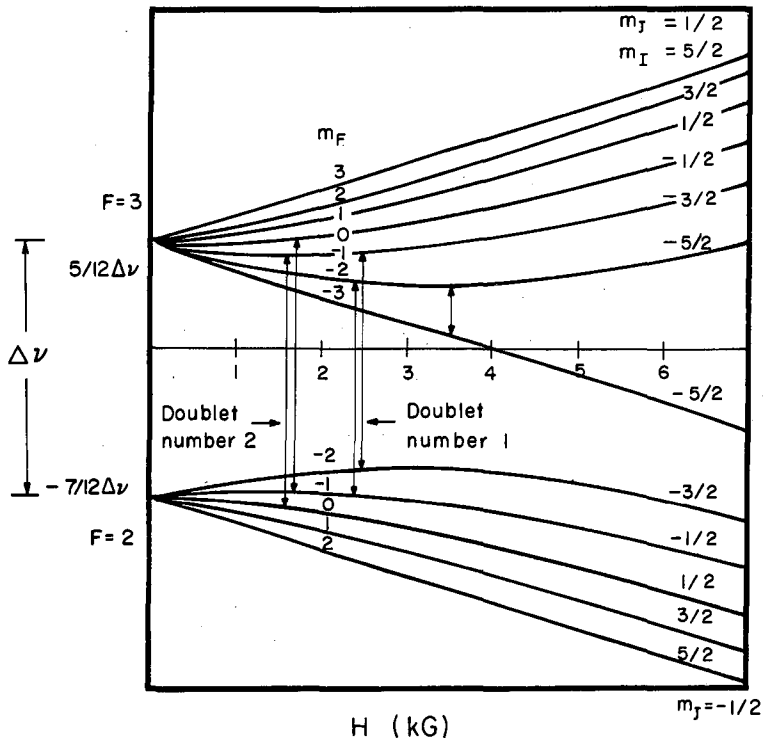

Fig. 1. Breit-Rabi diagram for Cs^{131} (μ_I = +3.52 nm).

field. One can calculate the derivative of the average of the doublet and locate a magnetic field for which

$$\frac{\partial \nu_{12}}{\partial H_0} = 0 . \qquad \text{(II. 13)}$$

Each of these frequencies, then, has only a quadratic dependence on the field in this region. This reduces the line width to the "natural line width" as discussed in Sec. V.

Taking the difference of the doublet frequencies, $\nu_{12} - \nu_{21}$, at the field-independent point, the separation becomes

$$\nu_{12} - \nu_{21} = 2g_I \frac{\mu_0 H_0}{h} , \quad \nu_{12} > \nu_{21}. \qquad \text{(II. 14)}$$

Measuring each frequency of the doublet and taking the difference of them results in an independent value of g_I. The error of the g_I measurement depends on the narrow linewidths of each frequency and the error in H_0.

Similarly, a calculation of the average of the doublet frequencies $(\nu_{12} + \nu_{21})/2$ results in it being proportional to $\Delta\nu$, and the explicit dependence on g_I is removed. By adding the two frequencies an independent value of $\Delta\nu$ results. These transitions are referred to as field-independent transitions; for this experiment these transitions are the ones that yield the most accurate values of g_I and $\Delta\nu$.

III. THEORY OF THE HYPERFINE STRUCTURE ANOMALY

The hfs splitting, as defined by Eq. (II.1), is the result of the electron interaction with the nucleus in the absence of an externally applied magnetic field. Its value has been estimated for a $^2S_{1/2}$-state electron interacting with a point nucleus by Fermi and Segrè (FER 33) to be

$$h\Delta\nu = \frac{16\pi\mu_0^2 g_I}{3} |\psi_s(0)|^2 (I+1/2), \qquad \text{(III. 1)}$$

where μ_0 is the Bohr magneton and $\psi_s(0)$ is the S-state electron wave function evaluated at the nucleus.

For two isotopes differing by two neutrons there results the approximate relationship

$$\frac{\Delta\nu_1}{\Delta\nu_2} = \frac{g_{I_1}(2I_1+1)}{g_{I_2}(2I_2+1)} \qquad \text{(III. 2)}$$

If, however, very accurate values of $\Delta\nu$ and g_I are obtained for the two isotopes, a deviation from this equality will be exhibited. This deviation is due in part to the finite size of the nucleus and to the interaction of the electron with the neutron and proton distribution within the nucleus. It is this latter deviation which is referred to as the hfs anomaly, and its measurement reflects the neutron-proton coupling within the nucleus. Formally, the above expression is written

$$\frac{\Delta\nu_1}{\Delta\nu_2} = \frac{g_{I_1}(2I_1+1)(1+\epsilon_1)}{g_{I_2}(2I_2+1)(1+\epsilon_2)} = \frac{g_{I_1}}{g_{I_2}} \frac{(2I_1+1)}{(2I_2+1)} (1+{}^1\Delta^2) \ , \qquad \text{(III. 3)}$$

where ${}^1\Delta^2 \approx \epsilon_1 - \epsilon_2$; ϵ_1 and ϵ_2 are the individual isotope hfs anomalies, but the quantity to be compared with measurement is ${}^1\Delta^2$. Isotope 1 is by convention the lighter of the two.

A theory was originally given by Bohr and Weisskopf and is sometimes referred to as the "Bohr-Weisskopf theory of the hyperfine structure anomaly" (BOH 50). It was extended by Eisinger and Jaccarino (EIS 58), and later by Stroke, Blin-Stoyle, and Jaccarino(STR 61).

The theory proceeds by treating the spin angular momentum of the protons and neutrons separately from the orbital angular momentum. Thus the electron moves in two vector potential fields, one due to the nuclear spins,

$$\underset{\sim}{A}_S(\underset{\sim}{r}) = \int \frac{\underset{\sim}{M}_S(\underset{\sim}{R}) \times (\underset{\sim}{r} - \underset{\sim}{R})}{|\underset{\sim}{r} - \underset{\sim}{R}|^3} \, d\underset{\sim}{R} \quad , \tag{III. 4}$$

and the other due to the nucleon orbital motions,

$$\underset{\sim}{A}_L(\underset{\sim}{r}) = \frac{e}{Mc} \int \frac{\phi^*(\underset{\sim}{R}) \underset{\sim}{P} \phi(\underset{\sim}{R})}{|\underset{\sim}{r} - \underset{\sim}{R}|} \, d\underset{\sim}{R} \quad , \tag{III. 5}$$

where

$\underset{\sim}{r}$ is the position vector for the electron,
$\underset{\sim}{R}$ is the position vector for the nucleon,
$\underset{\sim}{M}_S(\underset{\sim}{R})$ is the volume magnetization of nucleon spins,
$\underset{\sim}{P}$ is their velocity,
$\phi(\underset{\sim}{R})$ is the nucleon wave function.

The electron will react with these fields according to the Dirac theory for the electron, resulting in the energy

$$W = e \int d\underset{\sim}{r} \psi^*(\underset{\sim}{r}) \underset{\sim}{\alpha} \cdot \underset{\sim}{A}(\underset{\sim}{r}) \psi(\underset{\sim}{r}) \, , \tag{III. 6}$$

where $\psi(\underset{\sim}{r})$ is the electron wave function, e is the electronic charge, and α are the usual Dirac matrices.

By relating W above to W for a point dipole, one arrives at the definition of the single-isotope anomaly,

$$W = W(0)(1+\epsilon) \, . \tag{III. 7}$$

By integrating over the angular variables of the electron, it may be shown that

$$\epsilon = \frac{1}{\mu \int_0^\infty F_0 G_0 dr} \left\{ \int_N \sum_i d\tau_N \phi_N^* \left[g_S^{(i)} \left(S_z^{(i)} \int_0^{R_i} FG dr - D_z^{(i)} \int_0^{R_i} \frac{FGr^3}{R_i^3} dr \right) \right.\right.$$

$$\left.\left. + g_L^{(i)} L_z^{(i)} \int_0^{R_i} \left(1 - \frac{r^3}{R_i^3}\right) FG dr \right] \phi_N \right\} \, , \tag{III. 8}$$

where $F(r)$ and $G(r)$ are the Dirac radial wave functions for the electron in which the nuclear charge distribution must be specified. The quantities $F_0(r)$ and $G_0(r)$ are the same except that the nucleus is treated as a point charge. The superscript refers to the nucleons and

$$D_z^{(i)} = \frac{1}{2}\left[S_x^{(i)} \frac{3X_iZ_i}{R_i^2} + S_y^{(i)} \frac{3Y_iZ_i}{R_i^2} + S_z^{(i)} \left(\frac{3Z_i^2 - R_i^2}{R_i^2}\right)\right] \qquad \text{(III. 9)}$$

The nuclear charge distribution used (STR 61) for the determination of the Dirac radial wave function is a function representing a trapezoidal distribution of charge as described by Hahn, Ravenhall, and Hofstadter (HAH 56). By solving the Dirac equation with use of this potential, the functions F and G, F_0 and G_0 can be obtained and eventually the above radial integrals evaluated. The result is

$$\epsilon = -\frac{1}{\mu}\left(\int_N \sum_{i,n} d\tau_N \phi_N^* \frac{R_i^{2n}}{R_N^{2n}} \left\{g_S^{(i)}\left[S_z^{(i)}(b_S)_{2n} - D_z^{(i)}(b_D)_{2n}\right]\right.\right.$$

$$\left.\left. + g_L^{(i)} L_z^{(i)}(b_L)_{2n}\right\} \phi_N\right), \quad n = 1, 2. \qquad \text{(III. 10)}$$

The coefficients b_S, b_D, and b_L result from the radial integration and are tabulated by Stroke, Blin-Stoyle and Jaccarino (STR 61). The final step is to evaluate the expectation value by using the proper nuclear wave functions.

Several approaches to the evaluation of ϵ have been taken. First (BOH 50) the spin and orbital contributions are retained separately as

$$\mathcal{K}_S = \frac{\int_0^R FGdr}{\int_0^\infty FGdr} \qquad \mathcal{K}_L = \frac{\int_0^R (1 - \frac{r^3}{R^3}) FGdr}{\int_0^\infty FGdr}, \qquad \text{(III. 11)}$$

such that averaging over the nuclear parameter R, we obtain

$$\epsilon = -\bar{\mathcal{K}}_S a_S - \bar{\mathcal{K}}_L a_L \qquad \text{(III. 12)}$$

if the contribution to ϵ is from a single nucleon. The weighting functions are given by $a_S = \frac{g_S}{g_I}\frac{(g_I - g_L)}{(g_S - g_L)}$ and $a_L = 1 - a_S$. The assumption is made that the spin and orbital contributions to ϵ combine as the spin and orbital contributions combine in the moment $\underset{\sim}{\mu}_I$; i.e.,

$$a_S = \frac{\underset{\sim}{\mu}_S \cdot \underset{\sim}{I}}{\underset{\sim}{\mu}_I \cdot \underset{\sim}{I}}$$

and

$$a_L = \frac{\underset{\sim}{\mu}_L \cdot \underset{\sim}{I}}{\underset{\sim}{\mu}_I \cdot \underset{\sim}{I}} \quad . \tag{III. 13}$$

Then for two isotopes differing by two neutrons,

$$^1\Delta^2 = \epsilon_1 - \epsilon_2 = \overline{\mathcal{H}}_S - \overline{\mathcal{H}}_L \frac{g_L g_S}{g_S - g_L}\left(\frac{1}{g_{I_1}} - \frac{1}{g_{I_2}}\right) \quad . \tag{III. 14}$$

The approximations made are $\overline{\mathcal{H}}_{S1} \approx \overline{\mathcal{H}}_{S2}$, $\mathcal{H}_{L1} \approx \overline{\mathcal{H}}_{L2}$, $g_{S1} \approx g_{S2}$, and $g_{L1} \approx g_{L2}$. The values of $\mathcal{H}_S$ and $\mathcal{H}_L$ are obtained by assuming a homogeneously charged nucleus with a potential

$$V(X) = \left(\frac{3}{2} - \frac{1}{2}X^2\right)\frac{Ze}{R_0}, \quad X = \frac{r}{R_0} < 1.$$

Solving for F and G from the Dirac equation, the integrals are evaluated, and the result is

$$\mathcal{H}_S = b\frac{R^2}{R_0^2}, \quad \mathcal{H}_L = 0.62\ b\frac{R^2}{R_0^2}, \quad R_0 = 1.5\times10^{-13}A^{1/3}, \tag{III. 15}$$

where A is the mass number of the isotope. The coefficient b is a function of Z and is tabulated by Bohr and Weisskopf (BOH 50). The quantity $(R/R_0)^2$ must be averaged over the nucleus and a value of 4/5 is usually taken. It is the value between that for a uniform distribution (3/5) and that for a surface distribution (1). Finally, for a single particle for which

$$\underset{\sim}{\mu}_I = \underset{\sim}{\mu}_S + \underset{\sim}{\mu}_L$$

$$\underset{\sim}{\mu}_I = \mu_0 g_I \underset{\sim}{I} \ ,$$

$$\underset{\sim}{\mu}_S = \mu_0 g_S \underset{\sim}{S} \ , \qquad \text{(III. 16)}$$

and

$$\underset{\sim}{\mu}_L = \mu_0 g_L \underset{\sim}{L} \ ,$$

it follows that

$$g_I = g_L \pm \frac{1}{2L+1} (g_S - g_L) \quad \text{for} \quad I = L \pm \frac{1}{2} . \qquad \text{(III. 17)}$$

All quantities are specified in Eq. (III. 14), and $^1\Delta^2$ may be calculated and compared with experiment.

The functions F(r) and G(r) obtained above are actually power series in r. For a more accurate estimate of ϵ more terms may be retained and used in the evaluation of the integrals. Eisinger and Jaccarino (EIS 58) retain sufficient terms to reduce the error to a few percent. The results are

$$\overline{\mathcal{K}}_S = [(b_S)_2 + \zeta(b_S)_2'] R_{e2} - [(b_S)_4 + \zeta(b_S)_4'] R_{e4},$$

$$\overline{\mathcal{K}}_L = (b_L)_2 R_{e2} - (b_L)_4 R_{e4}, \qquad \text{(III. 18)}$$

where for the single nucleon

$$\zeta = \frac{2I - 1}{4(I+1)} \quad \text{for} \quad I = L + \frac{1}{2}$$

$$= \frac{2I+3}{4I} \qquad \text{for} \quad I = L - \frac{1}{2} . \qquad \text{(III. 19)}$$

The b and R coefficients are tabulated in the above reference, and the anomaly is again given by Eq. (III. 14)

As a final approximation to the evaluation of Eq. (III. 8), the CMT is applied to the calculation of ϵ (STR 61). Noya, Arima, and Horie (NOY 58) demonstrated the success of CMT in calculating the nuclear moments; and Stroke, Blin-Stoyle, and Jaccarino (STR 61) report

similar results in calculating the anomaly. It is therefore of interest to apply CMT to the calculation of the moment and the anomaly of Cs^{131}.

For the evaluation of ϵ, Eq. (III. 8) is used together with CMT in the evaluation of the expectation value of the right-hand side. The CMT employs the shell model concept of the nucleus, with the resulting single-particle configurations. These single-particle wave functions are taken as the ground state, and to these are added certain close-by admixtures. Formally, one writes for the nuclear wave function

$$\phi_n = \phi_0 + \sum_{i\neq 0} \beta(i)\,\phi_i \,, \tag{III. 20}$$

where the $\beta(i)$ are small mixing coefficients, and ϕ_i are the particular admixed configurations. The main restriction for the selection of ϕ_i results from the presumption that $\beta(i)$ is small, hence terms linear in $\beta(i)$ will be the largest contributions. By restricting the admixed configurations to those differing only by one single-particle state from ϕ_0, the condition of linearity in $\beta(i)$ will be met. Stroke, Blin-Stoyle, and Jaccarino (STR 61) have calculated the expectation value of Eq. (III. 8) and obtained

$$\begin{aligned} -\epsilon = \frac{1}{\mu}\Bigg(& a_S(\text{S. P.})\, g_S \left\{ (b_S)_2 \left[1 + \left(\tfrac{2}{5}\right)\zeta\right] \Im_1(\text{S.P.}) + (b_S)_4 \left[1 + \left(\tfrac{4}{7}\right)\zeta\right] \Im_2(\text{S.P.}) \right\} \\ & + a_L(\text{S. P.})\, g_L \left[(b_L)_2\, \Im_1(\text{S. P.}) + (b_L)_4\, \Im_2(\text{S. P.})\right] \\ & + \sum_i a_0^{(i)} \left\{ \left[(b_S)_2 \left(\tfrac{9}{10}\right) \Im_1(i) + (b_S)_4 \left(\tfrac{6}{7}\right) \Im_2(i) \right] g_S^{(i)} \right. \\ & \left. - \left[(b_L)_2 \Im_1(i) + (b_L)_4 \Im_2(i) \right] g_L^{(i)} \right\} \\ & + \sum_i a_2^{(i)} \left[\left(\tfrac{2}{5}\right) (b_S)_2 \Im_1(i) + \left(\tfrac{4}{7}\right) (b_S)_4 \Im_2(i) \right] g_S^{(i)} \Bigg) , \end{aligned} \tag{III. 21}$$

where

$$a_S(\text{S.P.}) = \frac{1}{2}\,, \quad a_L(\text{S.P.}) = J - \frac{1}{2}, \quad \zeta = \frac{2J-1}{4(J+1)} \text{ for } J = L + \frac{1}{2}\,;$$

$$a_S(\text{S.P.}) = -\frac{J}{2J+2}\,, \quad a_L(\text{S.P.}) = \frac{J(2J+3)}{2J+2}, \quad \zeta = \frac{2J+3}{4J} \text{ for } J = L - \frac{1}{2}\,.$$

The coefficients $(b_S)_2$, $(b_S)_4$, $(b_L)_2$, and $(b_L)_4$ were previously defined; however, they have been conveniently tabulated by Stroke, Blin-Stoyle, and Jaccarino. The radial integrals $\mathfrak{I}_1$(S.P.), $\mathfrak{I}_2$(S.P.), $\mathfrak{I}_1$(i), and $\mathfrak{I}_2$(i) are also tabulated according to the desired excitations. Again (i) stands for the various excitations considered. The three types considered are designated type I, II, and III. An example of each will be given. For a complete description, however, see Noya, Arima, and Horie (NOY 58) and Stroke, Blin-Stoyle, and Jaccarino (STR 61). (Note that J has replaced the symbol I; in the manner in which it is used it should cause no difficulty.)

Example 1.

Type I:

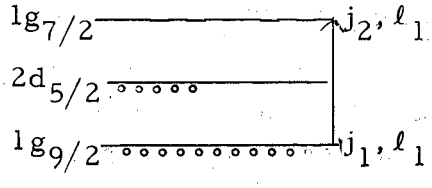

Proton contribution with $\Delta\ell = 0$ and $J = L + \frac{1}{2}$,

$J = \frac{5}{2}$, $L = 2$,

$j_1 = \ell_1 + \frac{1}{2} \rightarrow j_2 = \ell_1 - \frac{1}{2}$.

Example 2.

Type II:

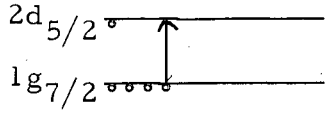

Proton contribution with $\Delta\ell = 2$ and $J = L + \frac{1}{2}$,

$J = \frac{5}{2}$, $L = 2$.

Example 3.

Type III:

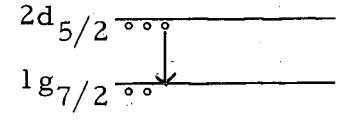

Proton contribution with $\Delta\ell = 2$ and $J = L + \frac{1}{2}$,

$J = \frac{5}{2}$, $L = 2$.

The complete list of excitations used in the calculation for cesium-131, -133 and -135 may be found in Sec. VI. The coefficients a are defined in Tables I through IV. In Table II $\ell_>$ is the larger of ℓ_1 and ℓ_2. All quantities are defined in Example 1 above except for n_1 and n_2. These are the number of particles in level 1 and 2, respectively. In Example 1, $n_1 = 10$, $n_2 = 0$. The values V_sI, ΔE, and $(V_t - V_s)$ are given by Stroke, Blin-Stoyle, and Jaccarino (STR 61).

Table I. a_0 for type I excitations.

Nucleus	J	Type I $a_0(\Delta\ell = 0)$		Contribution from even numbers of
Odd proton (neutron)	$L + \frac{1}{2}$	$\frac{n_1(2j_2 + 1 - n_2)}{2j_2 + 1} \frac{\ell_1(L+2)}{(2L+3)(2\ell_1+1)} \times$	$\frac{V_s I}{\Delta E}$	Protons (neutrons)
			$-\frac{(V_t - V_s)I}{2\Delta E}$	Neutrons (protons)
	$L - \frac{1}{2}$	$\frac{n_1(2j_2 + 1 - n_2)}{2j_2 + 1} \frac{\ell_1(L-1)}{(2L+1)(2\ell_1+1)} \times$	$-\frac{V_s I}{\Delta E}$	Proton (neutron)
			$\frac{1}{2}\frac{(V_t - V_s)I}{\Delta E}$	Neutron (proton)

Table II. a_2 for type I excitations.

Nucleus	J	Type I $a_2(\Delta\ell = 2)$		Contribution from even numbers of
Odd proton (neutron)	$L + \frac{1}{2}$	$\frac{n_1(2j_2 + 1 - n_2)3L}{8(2L+3)(2\ell_> - 1)} \times$	$\frac{V_s I}{\Delta E}$	Protons (neutrons)
			$-\frac{(V_t - V_s)I}{2\Delta E}$	Neutrons (protons)
	$L - \frac{1}{2}$	$\frac{n_1(2j_2 + 1 - n_2)3(L+1)}{8(2L+1)(2\ell_> - 1)} \times$	$-\frac{V_s I}{\Delta E}$	Protons (neutrons)
			$\frac{(V_t - V_s)I}{2\Delta E}$	Neutrons (protons)

Table III gives a_0 for Type II (an even number of n particles in orbit $j_1 = L + \frac{1}{2}$ into the odd group of p particles in orbit $J = L - \frac{1}{2}$) and for Type III (one of the odd p particles in orbit $J = L + \frac{1}{2}$ into the group of even n particles in orbit $j_1 = L - \frac{1}{2}$.

In order to calculate ϵ from Eq. (III.21), the magnetic moment μ must be calculated. The value of μ is given by

$$\frac{e}{2Mc} \left\langle \phi_N \mid g_S \underset{\sim}{S} + g_L \underset{\sim}{L} \mid \phi_N \right\rangle , \qquad \text{(III.22)}$$

where M is the mass of the protons. The CMT will provide the basis for the ϕ_N. Due to the difference between the operators ϵ_{op} and $\underset{\sim}{\mu}_{op}$, each excitation will make different contributions to the anomaly and the magnetic moment. Because of this, μ_I takes the simpler form

$$\mu_I = a_S g_S + a_L g_L + \sum_i a_0^{(i)} (g_S^{(i)} - g_L^{(i)}) , \qquad \text{(III.23)}$$

where for the odd proton

$$a_S = \frac{1}{2} , \quad a_L = J - \frac{1}{2} \quad \text{for } J = L + \frac{1}{2} ,$$

$$a_S = - \frac{J}{2J+2} , \quad a_L = \frac{J(2J+3)}{2J+2} \quad \text{for } J = L - \frac{1}{2} ,$$

and

$$g_S = \begin{pmatrix} 5.585 \\ -3.826 \end{pmatrix} \quad \text{for} \quad \begin{pmatrix} \text{proton} \\ \text{neutron} \end{pmatrix} ,$$

$$g_L = \begin{pmatrix} 1 \\ 0 \end{pmatrix} \quad \text{for} \quad \begin{pmatrix} \text{proton} \\ \text{neutron} \end{pmatrix} ,$$

and $a_0^{(i)}$ are the admixed matrix elements representing only $\Delta L=0$ excitations. The particular excitations used in the calculation of μ_I are discussed in Sec. VI. Like the anomaly the magnetic moment depends on the neutron-proton coupling, and together these calculations can aid one another in determining this coupling.

Table III. a_0 for type II and III excitations.

Type	a_0
II	$-\frac{n(2J-p)(L-1)L}{(2J-1)(2L+1)^2}\frac{V_s I}{\Delta E}$
III	$\frac{(p-1)(2j_1+1-n)(L+1)(L+2)}{(2j_1+1)(2L+1)(2L+3)}\frac{V_s I}{\Delta E}$

Table IV. a_2 for type II and III excitations.

Type	J	a_2	
II	$L+\frac{1}{2}$	$\frac{n(2J-p)}{1}\frac{3(L+1)}{8(2L+3)^2}\frac{V_s I}{\Delta E}$	$j_1 > J$
	$L-\frac{1}{2}$	$-n(2J-p)\frac{3}{8}\frac{L(L+1)}{(L-1)(4L^2-1)}\frac{V_s I}{\Delta E}$	$j_1 < J$
III	$L+\frac{1}{2}$	$\frac{(2j_1+1-n)(p-1)3(L+1)}{8(2L+3)^2}\frac{V_s I}{\Delta E}$	$j_1 > J$
	$L-\frac{1}{2}$	$-\frac{3}{8}\frac{(L+1)(2j_1+1-n)(p-1)L}{(L-1)(4L^2-1)}\frac{V_s I}{\Delta E}$	$j_1 < J$

IV. EXPERIMENTAL PROCEDURE

A brief picture of the operation of an atomic-beam machine is given, followed by a discussion of the preparation of the Cs^{131} sample. Finally, a detailed procedure is given for the measurement of $\Delta\nu$ and μ_I.

A. Atomic-Beam Method of Measuring the Hyperfine Interaction

The hfs, as mentioned earlier, is the result of $\underset{\sim}{\mu}_I$ and $\underset{\sim}{\mu}_J$ interacting with each other. In an atomic beam there is no interaction between atoms, and the interpretation of the interaction is relatively simple. The particular atomic-beam method to be described is the "flop-in" method; it results in a low-background experiment and provides a very sensitive method for the detection of radioactive nuclei such as Cs^{131}. For example, during one run the total number of atoms needed in the oven is only about 10^{11}.

The sample is prepared (see Subsec. IV. B) and placed in an oven at one end of an evacuated chamber. (For further details of the apparatus the reader is referred to Sec. V.) The oven is then heated to a temperature sufficient for the production of the atomic particles and the beam diverges from an oven opening. The beam is highly collimated and is directed through three collinear magnetic fields. The first and last magnetic fields, called A and B, respectively, are inhomogeneous deflecting fields. They are designed identical to each other and their gradients are in the same direction. The magnitude of these fields at the beam is approximately 10 000 G and on the Breit-Rabi diagram correspond to fields high enough for which there are only two values of $\partial W/\partial H$; i.e., $\mu_{eff} = \pm\mu_J$. Atoms in states with one μ_{eff} will be deflected opposite to those with the other sign, and therefore there will be two groups of atoms converging to the center of the machine from the diverging beam of the oven. If no transitions occur at the center of the machine, each atom will experience the same force in the B field as in the A field and hence will be deflected away from the center line of the machine. If, however, at the center of the machine an atom in a

state for which $\mu_{eff} = +\mu_J$ is changed to a state of opposite μ_J, then the deflection in the B magnet will be opposite to the deflection in the A magnet and the atom will be focused to the center line of the machine. For this purpose there is placed in between the A and B fields a magnet referred to as the C magnet. It is in this magnet that the radiofrequency perturbation is applied to the beam (through what is called a hairpin), thus causing atoms to change state. The atoms are then refocused when they pass through the B field. A detector is placed on the center line of the machine at the end opposite to the oven for the purpose of detecting the "flopped-in" beam.

In Sec. II, the transition frequencies were derived and show the dependence of the frequency on the value of the C field. This function depends in part on g_I, $\Delta\nu$, and the spin I. The process of measuring frequencies and magnetic fields in order to obtain g_I and $\Delta\nu$ (the spin has already been determined) is given below. By applying a radio-frequency signal ν, rotating in a plane perpendicular to the C field H_0, the transition will take place according to a transition probability. The transition-probability curve is symmetrically centered about the frequency ν_0. In the Zeeman frequency range, ν_0 is the Larmor frequency corresponding to H_0. The experimental data is obtained by fixing the C field at some value and varying ν. When the frequency is in the vicinity of that calculated in Sec. III, the detector will register those atoms that are focused. As the frequency is varied further the response of the detector will be as in Fig. 2. These curves are referred to as resonances and represent an overall transition-probability curve. The value of ν_0 is expected to be in the center of the curve. Field inhomogeneities can distort the resonances (see Fig. 3), and distortions give rise to large uncertainties in estimating ν_0.

Sections IV. C and IV. D will discuss the method of determining g_I and $\Delta\nu$ specifically.

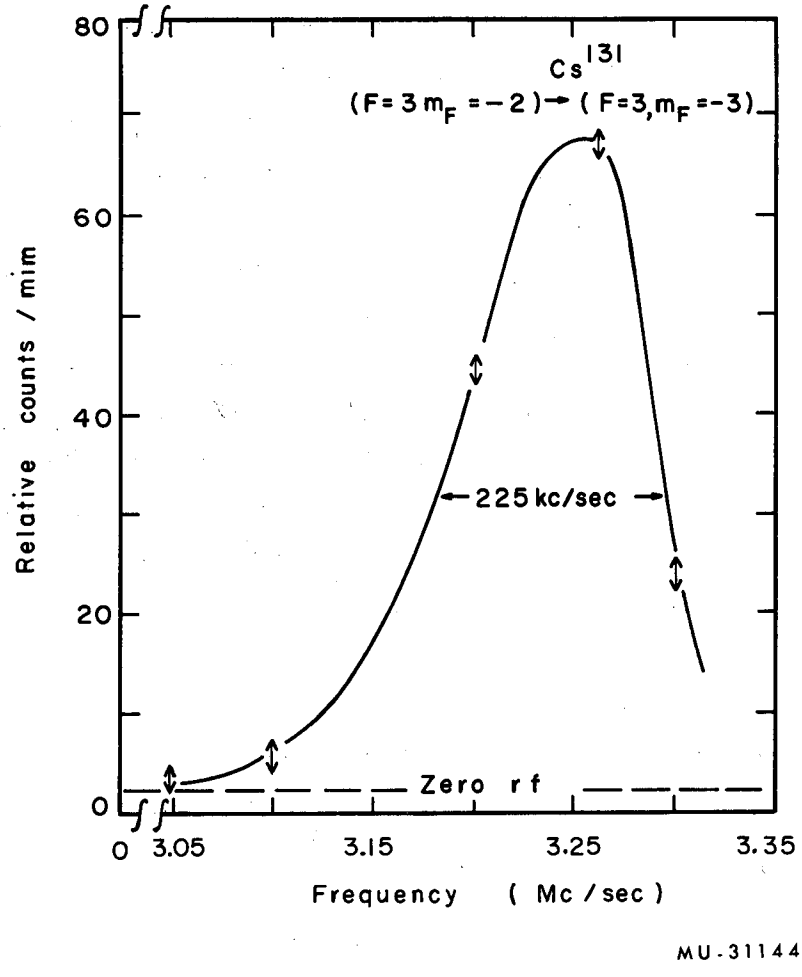

Fig. 2. $\Delta F = 0$ transition at 6.947 (64) G.

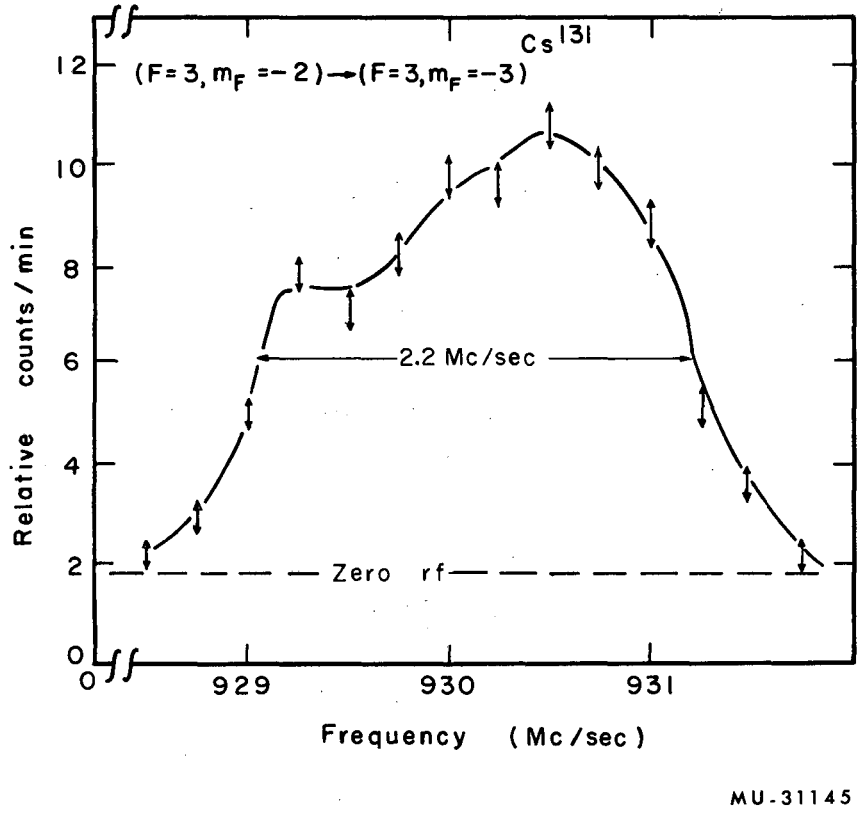

Fig. 3. $\Delta F = 0$ transition at 1499.58(12) G.

B. Sample Preparation

The particular choice of production was neutron bombardment on Ba metal; i.e.,

$$n + Ba^{130} \rightarrow Ba^{131} \rightarrow Cs^{131} \rightarrow Xe^{131} .$$

For this choice of production, the separation of Cs from Ba is relatively simple. Alternate production methods would be

$$_{54}Xe^{131}(p, n)_{55}Cs^{131}$$

and

$$_{54}Xe^{130}(d, n)\ _{55}Cs^{131},$$

but the activity per cubic centimeter of target is low since xenon is a gas. Also many other cesium isotopes would be produced along with Cs^{131}. Cesium-136 with a 13-day half-life would be among them and presents a problem of distinguishing it from Cs^{131}. The stable isotopes of Ba present in the metal are:

Isotope	% abundance	Cross section (barns)
Ba^{130}	0.10	0.024
Ba^{132}	0.097	7
Ba^{134}	2.42	< 4
Ba^{135}	6.59	5
Ba^{136}	7.81	< 0.1
Ba^{137}	11.32	4
Ba^{138}	71.66	0.5

The cross section for Ba^{130} is given by Yaffe, Kirsch, Standil, and Grunlund (YAF 49). The half-life of Ba^{131} is 11.6 days and that of Cs^{131} is 9.7 days. In each case the reaction proceeds by electron capture.

Due to the short half-lives of most of the products, the only ones of sufficient quantity or specific activity besides Ba^{131} and Cs^{131} are

Ba^{133} and Ba^{135}, with respective half-lives of 39 h and 29 h. These are sufficiently reduced a week after reactor shutdown so as not to interfere experimentally.

The facility used most frequently was the Experimental Test Reactor at Arco, Idaho. Typical operating conditions were:

Irradiation period = 23.7 days,
Thermal neutron flux = 5.1×10^{14} n/cm^2-sec,
Time-integrated flux nvt = 1.04×10^{21} n/cm^2.

A length of Ba metal rod (A. D. MacKay, Inc. 99.5% pure) was trimmed to fit within quartz tubing with dimensions 70.6 mm long, 1.9 mm outside diameter, with a 1-mm wall thickness. Quartz wool was packed into one end and this same end was sealed. A helium atmosphere was maintained during the sealing-off process. Figure 4 shows the capsule after sealing it off. This was then encapsulated in aluminum of 99.99% purity and shipped to Arco, Idaho. On its return the capsule was cut apart with the facilities of the Health Chemistry Group at the Lawrence Radiation Laboratory at Berkeley.

At this point the following chemistry was performed on the Ba metal by using the remote-handling facilities shown in Fig. 5.

a. Dissolve Ba metal in $H_2O + HCl$, resulting in $BaCl_2 + CsCl$. Add CsCl or RbCl as carrier.
b. Add $(Nh_4)_2CO_2$ and precipitate $BaCO_2$. Decant $CsCl + (NH_4)_2CO_2 + NH_4Cl$.
c. Evaporate to dryness and heat in furnace to sublime $(NH_4)_2CO_2 + NH_4Cl$.

The product remaining is CsCl (or RbCl). This is mixed with Ca metal and placed in the oven shown in Fig. 6. The final part of the chemistry is then the heating of the oven to a temperature sufficient for the reaction

$$CsCl + Ca \rightarrow Cs + CaCl.$$

This reaction takes place at about 350°C.

The only difficulty encountered was that usually there was a large quantity of NH_4Cl to sublime, and this must eventually be sent through the air filtering system of the remote-handling facility. Air filters

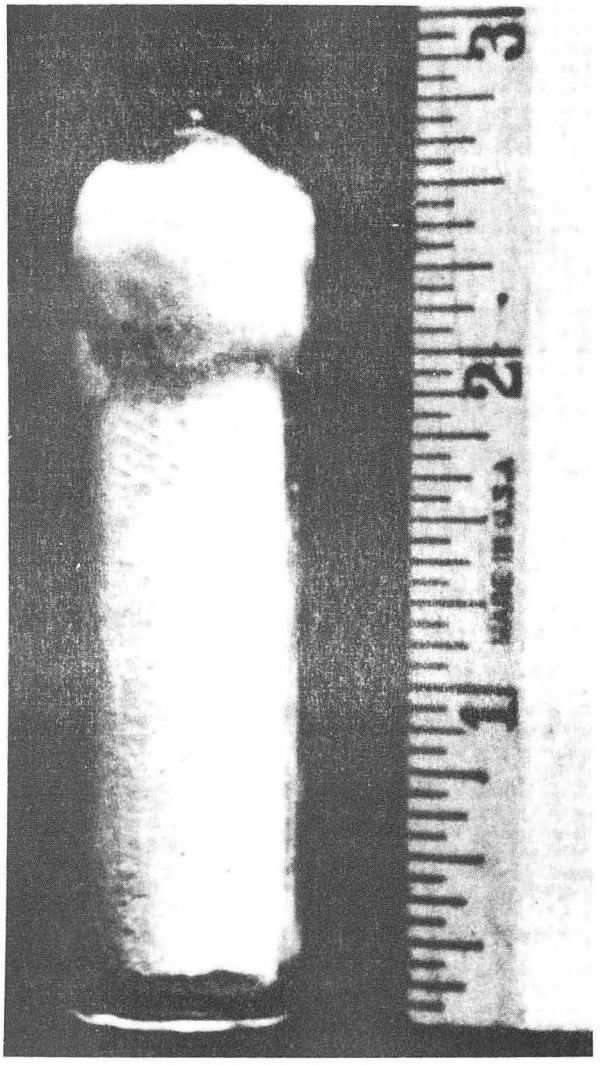

ZN-3809

Fig. 4. Barium metal encapsulated in quartz tubing.

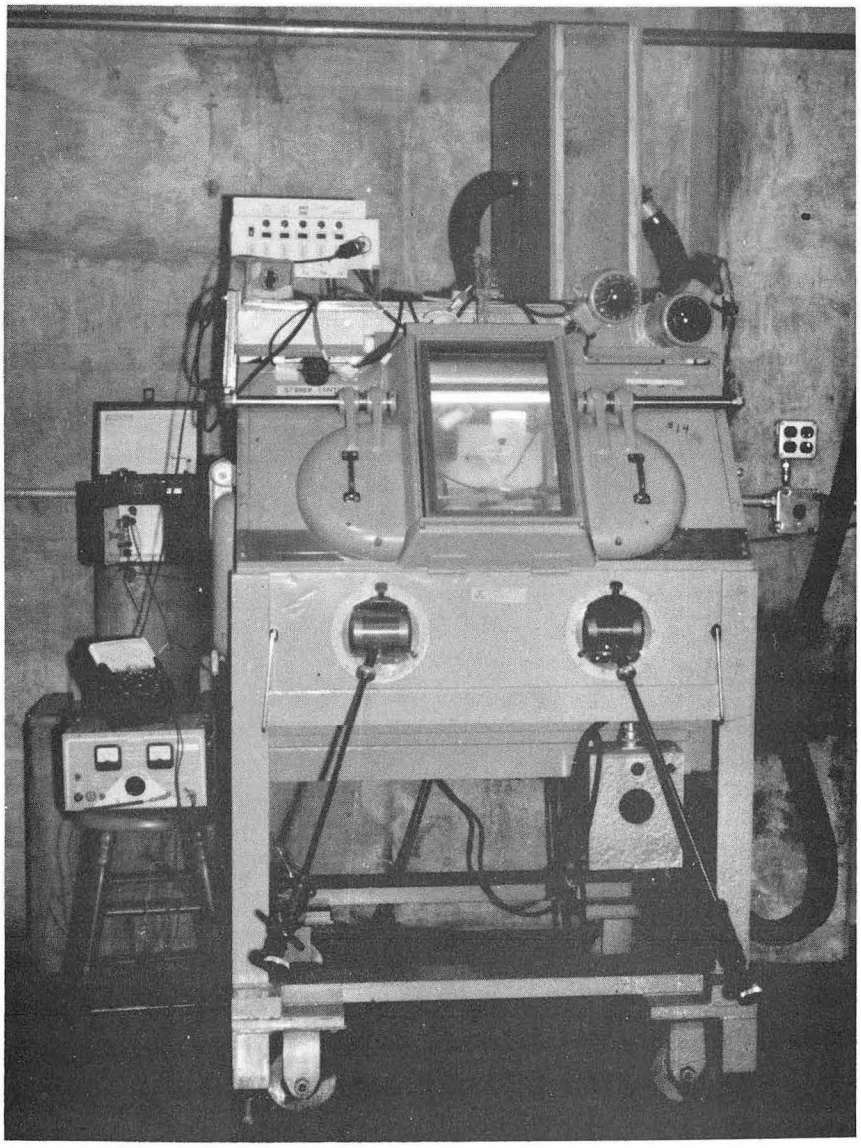

ZN-2366

Fig. 5. Remote-handling facilities.

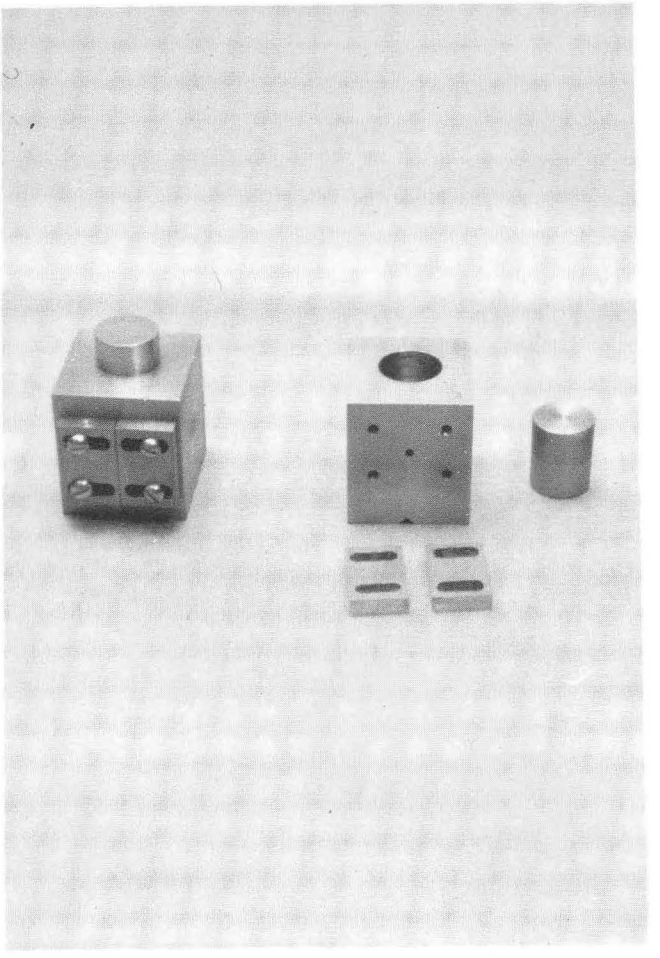

ZN-2391

Fig. 6. Stainless steel ovens.

clogged in 30 min and eventually it was necessary to pass the sublimed vapor through water first to absorb some of the NH_4Cl. This greatly increased the lifetime of the filter.

The chemistry took about 20 h, due mainly to the large quantity of Ba metal (30 g) processed and to the awkwardness of the remote-handling facility.

Concerning the production of Cs^{131} within the reactor, these results easily follow from the usual buildup considerations:

(a) For Ba^{131}, in atoms per gram of Ba metal (t in days),

Bombardment in the reactor:

$$N(t) = 3.85\times10^{14}\ (1 - e^{-0.0597t})$$

(b) For Ba^{133}

Bombardment in the reactor:

$$N(t) = 2.58\times10^{13}\ (1 - e^{-0.427t})$$

(c) For Ba^{135}

Bombardment in the reactor:

$$N(t) = 6.36\times10^{14}\ (1 - e^{-0.577t})$$

(d) For Cs^{131}

Bombardment in the reactor:

$$N(t)=2.3\times10^{13}[14(1-e^{-0.0714t})+85.5(e^{-0.0714t}-e^{-0.0597t})]$$

After shutdown of the reactor:

$$N(t)= N_1(T)e^{-0.0714t}-5.1\ N_2(T)\,(e^{-0.0714t}-e^{-0.0597t}).$$

Where T is the bombardment time in days and t is the time after shutdown in days. N_1 and N_2 are the number of atoms/gm of Ba-metal of Cs^{131} and Ba^{131} respectively. From these results, we see that Ba^{133} and Ba^{135} saturate in about 10 days of bombardment, whereas saturation of Ba^{131} and Cs^{131} does not occur until about 2 months. The buildup of Ba^{131} and Cs^{131} is shown in Fig. 7.

From the shutdown relationship for Cs^{131} we see the possibility of "milking" the sample; i.e., after the first chemistry the Ba precipitate decays to Cs^{131} and at the appropriate time another chemistry is performed. It is possible to have several experiments from one bombardment. The best time for milking is about 15 days after each

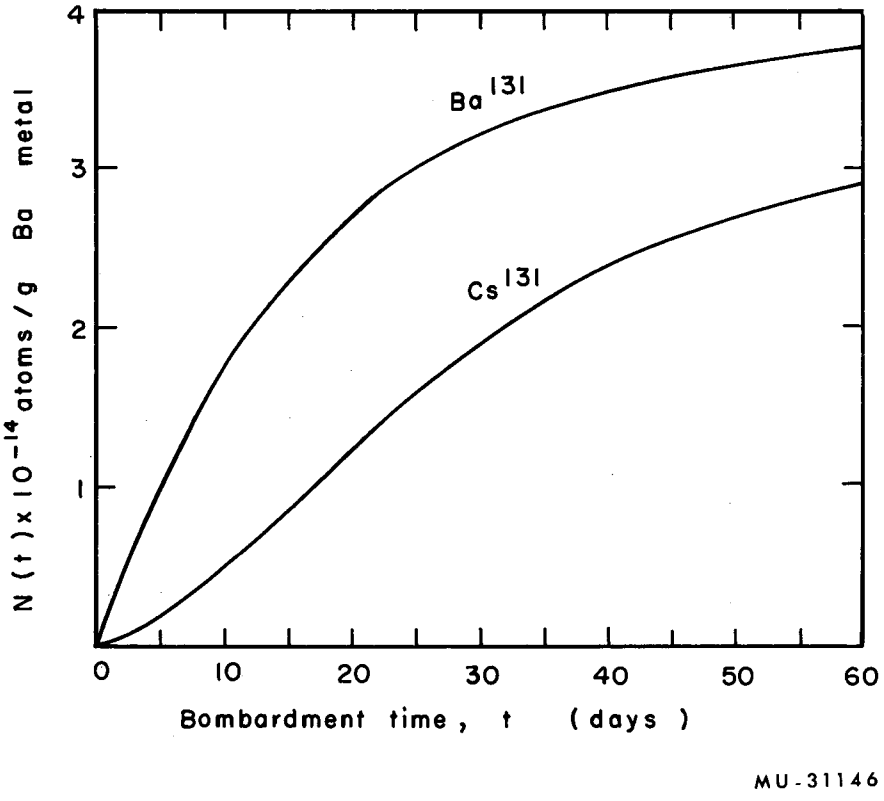

Fig. 7. Production of Ba^{131} and Cs^{131}.

chemistry. The first milking after the first chemistry will produce about one-fifth the activity of the first chemistry.

The activity involved in a sample results, as mentioned above, mainly from Cs^{131} and Ba^{131}. Since their decay rates are approximately the same, the relative activity between the two is based on their respective total decay energy. There is about a 3:1 ratio in total decay energy; therefore, Ba^{131} produces about three times the dose rate of Cs^{131}. This-together with the fact that the total decay energy is low (0.32 MeV) in Cs^{131}-results in very low dose rates emanating from the oven so there is not a major shielding problem here. Typical values are: the sample may produce 10 roentgen/h (R/h) at 1 in. After the separation from Ba the sample produces about 3 R/h at the same distance; with the sample in the oven the dose rate 1 in. away is about 50 mR/h. The oven chamber itself provides adequate shielding.

C. Measurement of $\Delta\nu$ at Low Frequencies

From the Breit-Rabi diagram (Fig. 1) the transition $(F = 3,\ m_F = -2) \rightarrow (F = 3,\ m_F = -3)$ is one that can be focused, and in fact the frequency is given by Eq. (II.12),

$$\nu \approx \nu_0 + \nu_0^2 \frac{2I}{\Delta\nu} \quad ,$$

with H_0 in gauss and all frequencies measured in Mc/sec. This relationship at low fields shows that ν does not depend sensitively on $\Delta\nu$, and that the dependence increases with increasing H_0. This suggests a starting point for the experiment.

Bellamy and Smith (BEL 53) report the following values for Cs^{131}:

$$\begin{aligned} \Delta\nu &= 13{,}200\,(110)\ \text{Mc/sec}, \\ \mu_I &= +3.48\,(4)\ \text{nm}, \\ I &= 5/2\ . \end{aligned} \qquad \text{(IV.1)}$$

If for the moment we neglect errors in determining the field H_0, the largest uncertainty in ν from Eq. (II.12) is due to $\Delta\nu$; i.e.,

$$|\delta\nu| = \nu_0^2 \frac{2I|\delta(\Delta\nu)|}{(\Delta\nu)^2} \quad , \tag{IV.2}$$

where $\delta\nu$ is the region through which the frequency will be varied to locate the resonances. This region would be very large at high fields and the resonance would be more difficult to locate, especially for radioactive nuclei. For radioactive nuclei the detector is a "button" to collect the focused atoms–requiring exposure times in the beam of from 5 to 10 min for each frequency setting. Therefore, any aid in locating the resonance is important. For example, the experiment should begin at low fields since this reduces $|\delta\nu|$. Also, one can sometimes increase the line width by decreasing the length of the hairpin (see Sec. V) and thereby help to locate the resonance within $\delta\nu$. However, as will be seen, one eventually wants a narrow line, to decrease the error of ν as much as possible.

Using the values given in (IV.1), the first sweep range ${}^1_c\delta\nu$ can be calculated from (IV.2). The superscript refers to the experiment and c indicates calculated value. At low fields the line widths are small; hence the locating of ν produces a new error ${}^1_m\delta\nu$, obtained from the line shape (m indicates a measured value). Substitution of this back into the above formula produces a new value of ${}^2_c\delta(\Delta\nu)$ at the same magnetic field at which the experiment was run. Now an increase in the magnetic field in the same formula increases the sweep range ${}^2_c\delta\nu$. This frequency is measured at the higher field and ${}^2_m\delta\nu$ is determined; then a new value of ${}^3_c\delta(\Delta\nu)$ is calculated, and so on. Each time $\delta(\Delta\nu)$ becomes smaller. As the field is increased further the above formula ceases to be valid due to the fact it is an expansion in H_0. Terms in g_I now enter, as can be seen from the formula for the frequency in intermediate fields [Eq. (II.11)]. An approximate value of g_I is necessary; it may be estimated from the Fermi-Segrè formula to within about 1%,

$$\frac{\Delta\nu_1}{(g_{I_1})(2I_1+1)} \approx \frac{\Delta\nu_2}{(g_{I_2})(2I_2+1)} \quad , \tag{IV.3}$$

with Cs^{133} as the comparison isotope. Computer techniques may be used to advantage (as discussed later) in this intermediate-field region. Eventually the error in $\Delta\nu$ will be more dependent on g_I and it becomes desirable to have an independent determination of g_I. This can be done using certain of the $\Delta F = \pm 1$ transitions discussed later.

In all of the formulae a value of H_0 and its error are specified. These values are obtained by calibrating the C field during the experiment. Material used for calibration, such as RbCl or CsCl, is placed in the oven along with the radioactive isotope, then the stable isotope is detected by a hot-wire detector. For isotopes used in calibration the constants g_I and $\Delta\nu$ are very accurately known, and observation of a resonance of fairly narrow line width determines the field H_0. In some cases, depending on the sensitivity of the results to changes in field, the usual magnetic-field regulation is sufficient; all that is necessary is calibration before and after the experiment. Errors in short-term and long-term variations are easily estimated. There are cases where continuous monitoring of the magnetic field is necessary. One way to accomplish this is by observing the calibrating resonance continuously and either manually correcting the field to maintain this resonance or electronically locking the magnetic field to the resonance shape. This type of electronic lock is described in detail by Braslau (BRA 60).

Usually, the hot wire detecting the resonance obstructs the radioactive detector to a certain extent, since both are on the center line of the machine. This can be kept to a minimum by keeping the cross-sectional area of the hot-wire filament small. Another way, just as satisfactory, of monitoring the magnetic field continuously is by using a nuclear magnetic resonance (NMR) probe and accompanying instrumentation (for example, the Harvey Wells Corp. model 502).

The procedure is to fix the probe somewhere within the homogeneous field and monitor its resonance on a convenient oscilloscope. A single calibration with the beam will suffice to calibrate the probe; then monitoring the NMR probe oscilloscope will be equivalent to monitoring the magnetic field. A maximum error of 0.05 G for a field of 2500 G is easily obtained.

The experiment continues at successively higher fields until the error in $\Delta\nu$ becomes a few megacycles, at which time it is more convenient to use $\Delta F = \pm 1$ transitions.

D. Independent Measurement of $\Delta\nu$ and g_I

There are two main features of a direct transition, i.e., a transition for which $\Delta F = \pm 1$. The first feature is demonstrated by Eq. (II. 7). At very low magnetic fields the frequency of transition is approximately $\Delta\nu$. One would expect to be able to measure $\Delta\nu$ exactly by just such a transition; however, at zero fields there are also the Majorana transitions (MAJ 32). These transitions can occur within the C magnet and between the magnets where the fields are rapidly changing both direction and magnitude. These transitions may cause unpredictable changes in the background and therefore H_0 is usually maintained above a few gauss. In addition sufficient power could not be obtained above 12.4 kMc/sec due to the cutoff frequency of the Hewlett-Packard traveling-wave tube amplifier, model 495A. And, in order that resonant frequencies be less than 12.4 kMc/sec the magnetic field must be greater than 636 G. The first direct transition was obtained at this field.

The second feature of the direct transition is the existence of doublets near field-independent points. These doublets have already been mentioned in Sec. II. It was seen that in measuring each of the doublet frequencies, the difference between the frequencies is proportional to μ_I and the sum of the frequencies is proportional to $\Delta\nu$. Likewise at the field-independent point the lines are very narrow. There are two such doublets for Cs^{131}, which are given in Table V.

Table V. Cesium-131 field-independent doublets.

Doublet No.	Level 1	Level 2	Frequency (Mc/sec)	Separation (Mc/sec)	H (G)
1	F=3, m_F=-2	F=2, m_F=-1	11343.6	5.2	2440
	F=3, m_F=-1	F=2, m_F=-2	11338.4		
2	F=3, m_F=0	F=2, m_F=-1	12989.3	1.7	808
	F=3, m_F=-1	F=2, m_F=0	12991.0		

The higher-frequency doublet was not examined since, again, the frequency is higher than the cutoff frequency of the rf circuits. Also, doublet No. 1 has the larger separation and therefore has the smaller fractional error in the separation for a given error in line width. This will give the smallest fractional error in the moment μ_I.

Up to this point in the experiment, $\delta(\Delta\nu)$ is approximately a few megacycles, which means that the frequencies are uncertain by about this amount. The doublet is in a field-independent region and hence these lines are very narrow (approximately 15 kc/sec). It is therefore necessary to reduce the field and broaden the lines in order to facilitate locating the resonance.

The experiment progresses by measuring frequencies in the region of magnetic field $630 \leq H_0 \leq 2500$ G until the uncertainty in $\Delta\nu$ is approximately 50 kc/sec. At this time the doublet may be located. The difference and the sum of the doublet may then determine $\Delta\nu$ and g_I independently, and the anomaly may be calculated [Eq. (III.3)].

To ensure that the value of $\Delta\nu$ and g_I obtained is consistent with all resonances and not just the doublet, a computer routine called HYPERFINE 3 was used (see Subsec. IV.E). This routine calculates "best fit" values of $\Delta\nu$ and g_I that depend on all the experimental points. These best-fit values are the ones reported.

E. Computational Analysis

At the completion of a run the data must be processed for the next run. For this computation the IBM 7090 digital computer was used. There are two stages to the calculation. The first stage is to incorporate the most recent data with all the previous data to yield a better value of $\Delta\nu$ and g_I, This computer routine is called HYPERFINE 3 and was written by Zurlinden (ZUR 59). The computation proceeds as follows: Frequencies with their errors as measured from the runs are input data, along with errors in magnetic fields and all known constants for the calibrating isotopes. Essentially, all quantities and their errors of Eq. (II.11) are specified except g_I and $\Delta\nu$. The computer will vary these two quantities to yield a value and an error for g_I and $\Delta\nu$ that best fit the input frequencies. It also assigns the most weight to the narrowest frequency. Once the best-fit values of $\Delta\nu$ and g_I are known the second stage of the calculation may begin; i.e., the calculation of frequencies as a function of magnetic field for any transition of interest. These tables, based on new constants, can be used to predict future operating frequencies. Frequency errors are also calculated in the same routine. This latter routine is called F-TABLE and was written by Ewbank (EWB 61).

V. APPARATUS

Section IV discussed the overall operation of an atomic-beam machine; this section discusses the component parts of the machine separately and in more detail. When the field-independent doublet $\Delta F = \pm 1$ was examined, the resonances were not symmetrical but exhibited "structure" (see Sec. VI). This was seen many times for Cs^{133}. We decided that the usual strap hairpin would not operate adequately at these frequencies and that the proper solution would be a waveguide hairpin. Unfortunately, the atomic-beam machine referred to as I, used for the earlier part of the work, had a C-magnet gap of 1/4 in. between the poles. We felt that tapering of the guide and cutting of a beam hole in the small dimension of the guide would disrupt the mode, again resulting in poor line shape. Alteration of the magnet would be too time consuming. There was another atomic-beam machine, referred to as VI, nearing completion and almost in operation. Its magnet gap is 1-3/4 in., and is sufficient for insertion of an x-band waveguide between the poles. Construction of the hairpin and the checkout of the machine took about one month. Low-frequency resonances were measured on machine I and the high-frequency measurements were made on machine VI; they will be discussed in this sequence.

A. Atomic-Beam Machine I and Low-Frequency Equipment

The atomic-beam machine I (Fig. 8) used in the low-frequency experiments has been described in detail by Braslau (BRA 60). It first becaume operational for atomic beams in 1958, and only minor modifications have been made since then. The general layout of the machine is shown in Fig. 9; the dimensions, however, may be found in the above reference.

The vacuum system was maintained by a total of five oil diffusion pumps followed by a Welch Duo-Seal mechanical pump. The pumps were distributed as follows: two Consolidated Vacuum Corp. MCF-700 pumps for the main can and one for the oven chamber, and a Distillation Products Inc. VMF-260 pump for the buffer chamber. These pumps

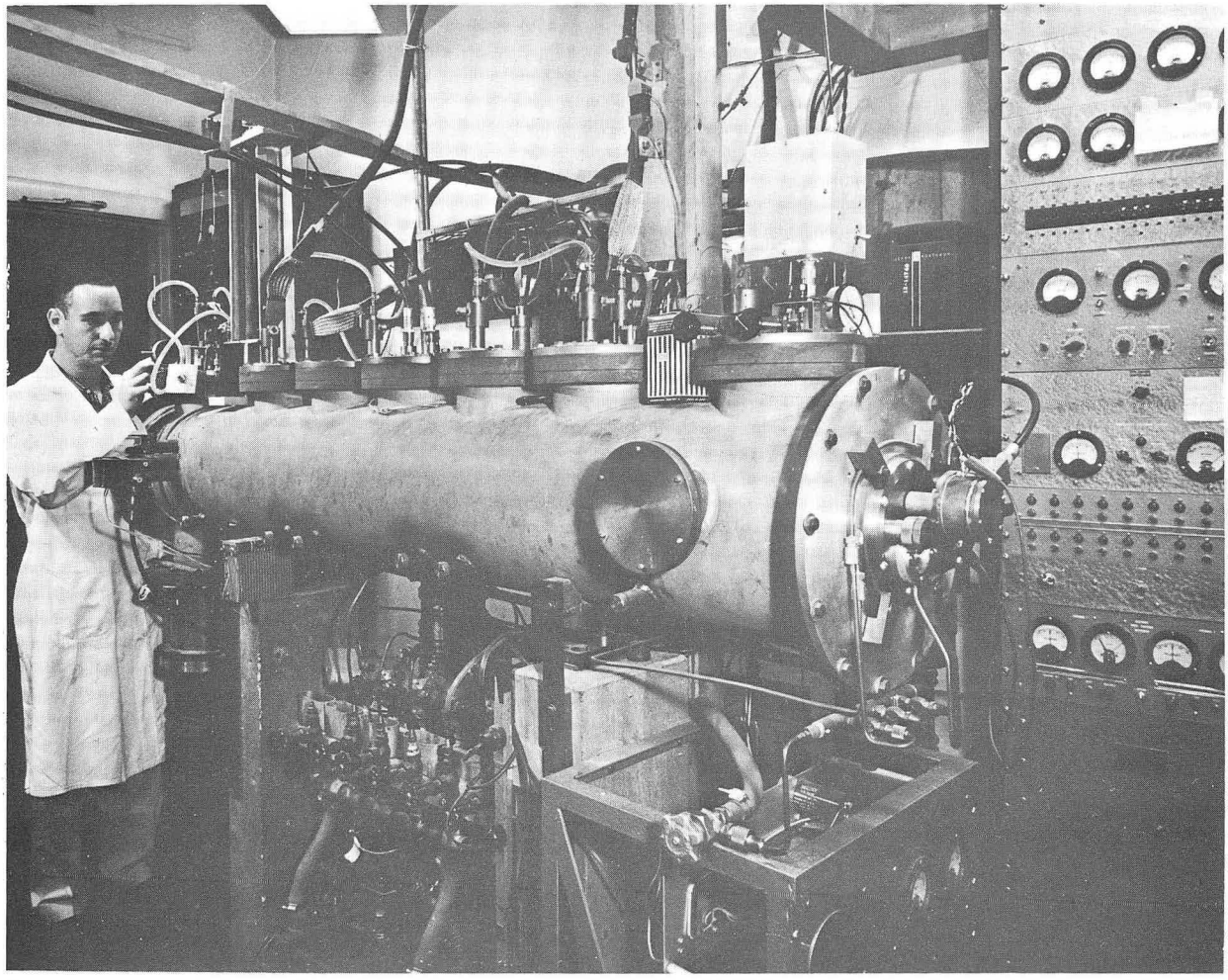

ZN-2055

Fig. 8. Atomic-beam machine I.

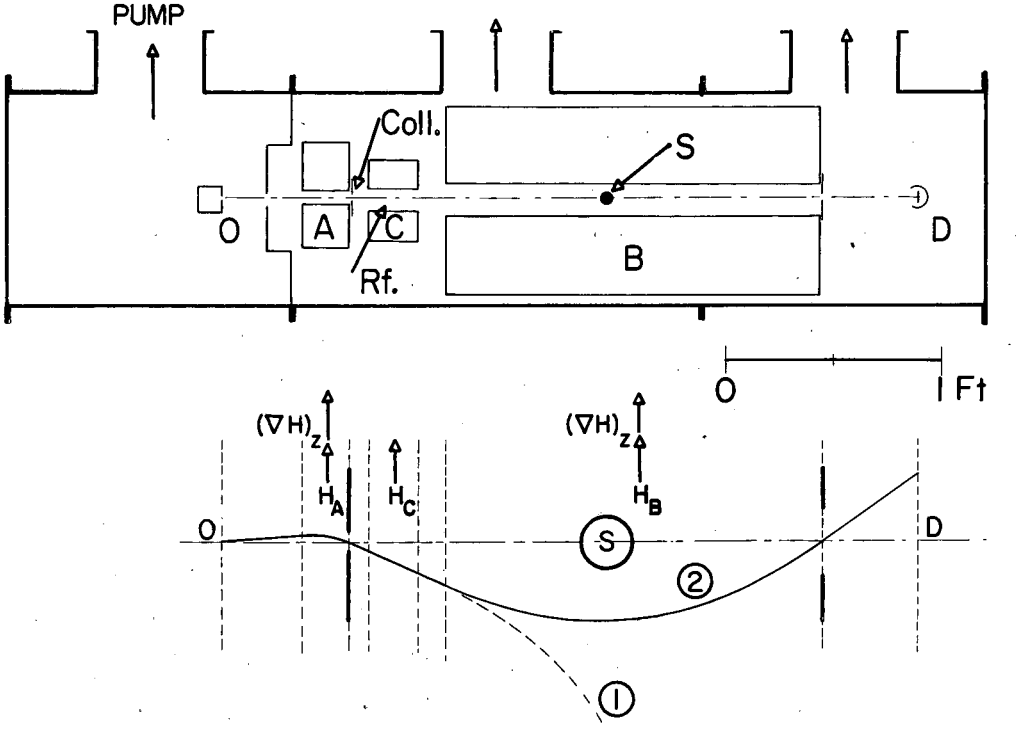

Fig. 9. General layout of an atomic beam machine.

fed into a Consolidated Vacuum Corp. MCF-300 pump which in turn fed into the mechanical pump. Pressures obtainable in the main can were approximately 2×10^{-7} mm Hg. In the oven chamber the pressure was about 3×10^{-6} mm Hg during the experiment.

The ovens used to contain the sample in the machine were approximately a 1-in. cube and were made of stainless steel (Fig. 6). The 1/8-in. jaws mounted on the front of the oven were separated by a 5-mil opening which formed the collimated beam. The chemistry was performed in the remote-handling facility of Fig. 5, and then the sample was loaded into the oven. It was then transferred to the machine and placed in the machine by way of a vertical oven-loader. This loader is essentially a series of pump-outs through which the oven may be taken from atmoshperic pressure to the oven chamber pressure of 3×10^{-6} mm Hg in about 15 min. The oven-heating element is a V-shaped filament just in front of the oven slit. With a few amperes flowing in the filament, a few hundred volts are placed across the filament and the oven. By means of electron bombardment the oven is heated to a few hundred degrees centigrade. The large mass of the oven and its heat capacity result in about an 8-min temperature response time.

In the main can are located the A, B, and C magnets and also the detectors. The A and B deflecting magnets have a cross-sectional shape as in Fig. 10. They are 17.5 in. long, water-cooled, and of the low-impedance type. Originally they carried 350 A at 4 V from a bank of submarine batteries. However, the $\Delta\nu$ of Cs^{131} is so large that in order to maintain the magnets in the high-field region of Fig. 1 the voltage was doubled to 8 V. This produced about 7000 G at the beam position.

The magnets were not yet saturated and the gradient at the beam position was maintained approximately equal to the value of the field there. Therefore, the overall operational design point was not disturbed appreciably as a result of this increase in voltage. The C magnet is a parallel-pole low-impedance homogeneous magnet; it is water cooled. The two pole faces are 2 in. high and 15-5/8 in. long with a 1/4-in. gap

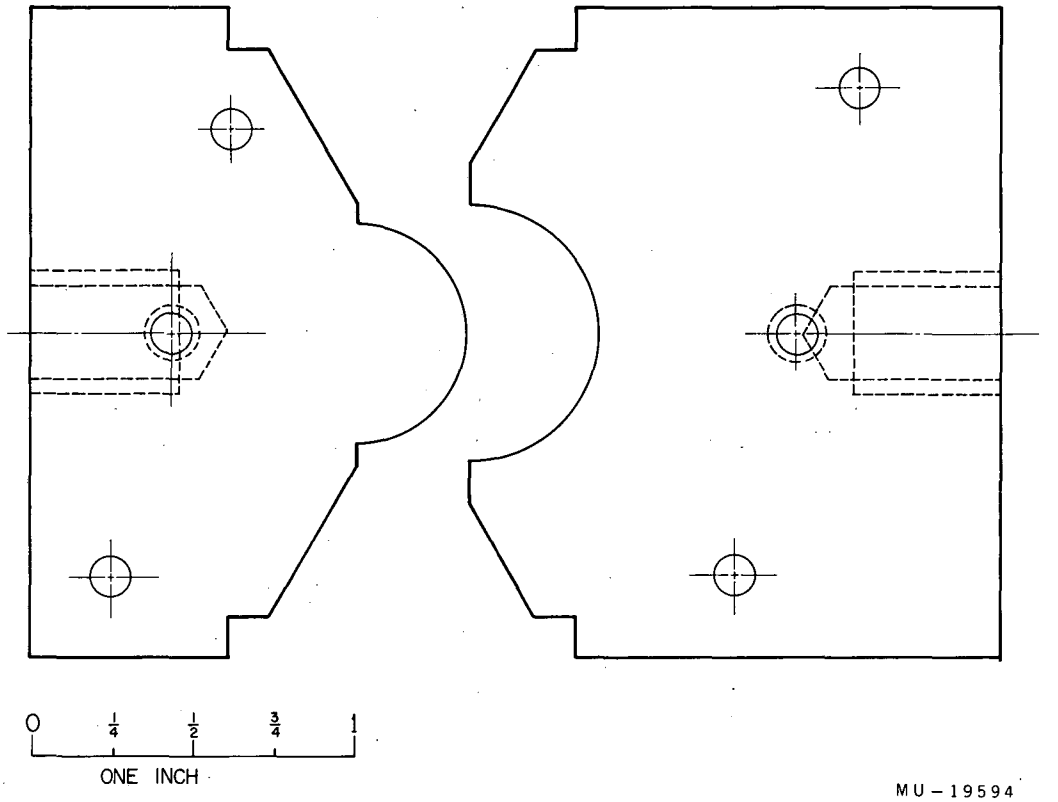

Fig. 10. A and B magnet cross section.

between them. The C magnet is also suppled by a bank of submarine batteries but it can be varied continuously through the use of resistances and a reversing switch.

In the detector chamber there are two hot-wire detectors to detect the stable beam, and a "button-holder" on the axis of the machine to collect the radioactive atoms. This button-holder may be loaded with a button outside the machine and rotated into the path of the beam through pumpouts in about 1 min. The buttons are made of brass with a sulfur coating for collection. A diagram of the button may be found in Fig. 11. The hot-wire detectors are of the filament-plate type. The beam atoms strike the hot wire, and, since the work function for the wire is greater than the ionization potential of the atoms, the beam atoms are ionized. A voltage accelerates the ions to the plate, resulting in a small flow of current. This current is detected by a micromicroammeter (Keithley model 410). Both detectors have a transverse motion (with respect to the beam direction) that is adjustable from outside the machine. Usually one detector monitors the flopped-out beam while the other is on the center line of the machine monitoring the calibration resonance.

The approach in all the experiments is one of basing the frequency stability on a very stable 1-Mc/sec crystal oscillator (James Knight Co. JKFS-1100). Its stability is 5 parts in 10^{10} per day. All oscillators are locked in some way, usually phase-locked, to this crystal. In the low-frequency region of the experiment the Tektronix, Inc. type 190B and the Hewlett-Packard model 608C oscillators are used directly. For more stability the Schomandl ND5, NB7, and NDF2 combination may be used, and is the first oscillator thus far mentioned which is phase-locked to the crystal. For the frequency range above 500 Mc/sec the Gertsch Products, Inc. AM-1, FM-4 combination may be locked to the crystal. Considerable power ($\leq$ 1 W) is needed because of high loss in transmission and impedance mismatch, especially at the hairpin itself. This power is supplied through traveling-wave amplifiers either obtained commercially or constructed locally around a given traveling-wave tube. Multiplication of frequencies is usually accomplished with crystal diodes of the type 1N21 or 1N23. Line stretchers and tuning stubs are used in

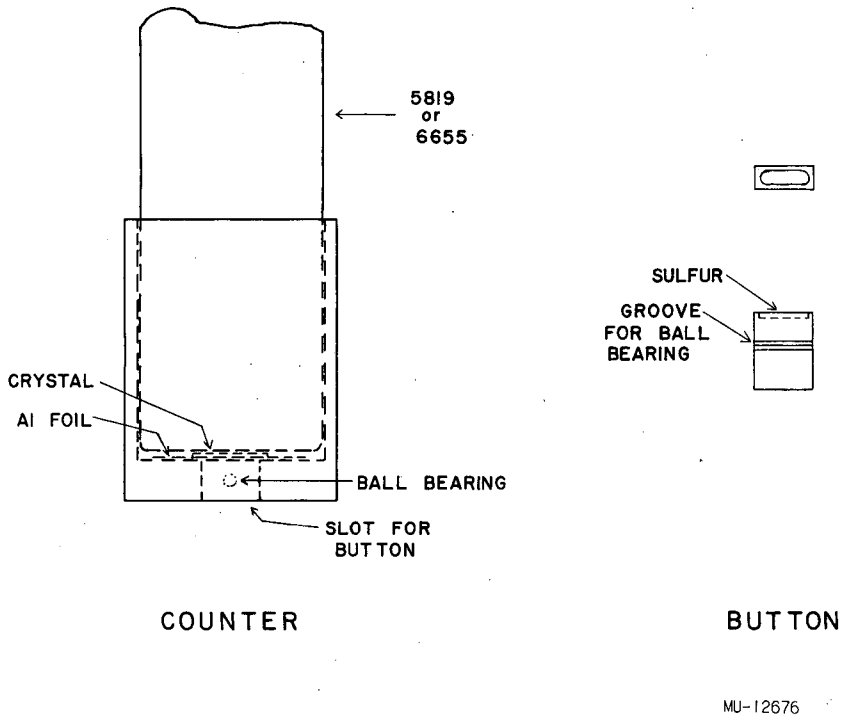

Fig. 11. Crystal counting head and button.

ample quantity throughout the circuit in order to obtain adequate power output. Usually one must set up three separate electronic circuits for each experiment. The search frequency, calibration frequency, and field-monitoring frequency are needed. A block diagram of a typical electronic circuit is shown in Fig. 12.

For each experiment, two hairpins are used. One is used for the search and calibration frequency and the other is used for field-monotoring. Strap hairpins of the type in Fig. 13 work well at low frequencies. The beam passes through a shorted piece of coax so as to intercept an oscillating magnetic field whose direction is parallel to the beam and hence will cause the π transitions mentioned in Sec. II. Torrey (TOR 41) shows that the natural line width for an optimum magnetic field is given by

$$\delta\nu = 1.07\,\frac{a}{\ell} \quad ,$$

where a is the most probable velocity of the atom and ℓ is the length of the oscillatory field along the beam. Then different hairpins of different lengths will give different line widths. Unfortunately this assumes a purely homogeneous field. Due to field inhomogeneities, which are always present, the lines become very broad and are almost independent of the length of hairpin. It is this fact that gives rise to the statement that the lines becomes broad at high fields. The true natural line width may be exhibited at field-independent points, since about those points the resonances are not sensitive to field changes that occur in the space about the hairpin. A double-oscillating-field hairpin (a Ramsey hairpin) was constructed. For details in the excitations of transitions by this method see Ramsey (RAM 56).

Qualitatively, the atom undergoes half the transition in the first oscillating field and the other half in the second oscillating field. The condition for such an effect is that the average field in between the two oscillating fields must be equal to the field at the two oscillating fields. The Ramsey hairpin may be seen in Fig. 14.

The magnetic field (C field) was measured and found to be sufficiently homogeneous that a Ramsey pattern should be observed. A considerable

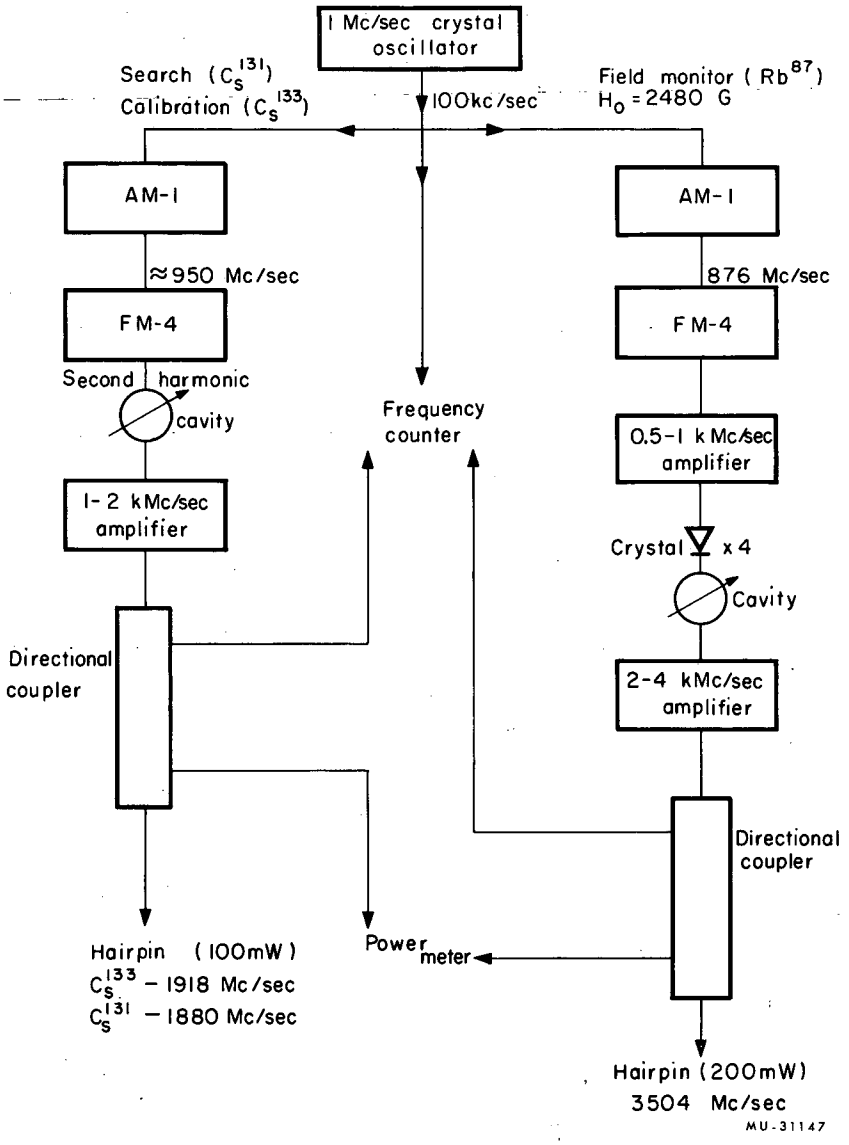

Fig. 12. Electronic circuit.

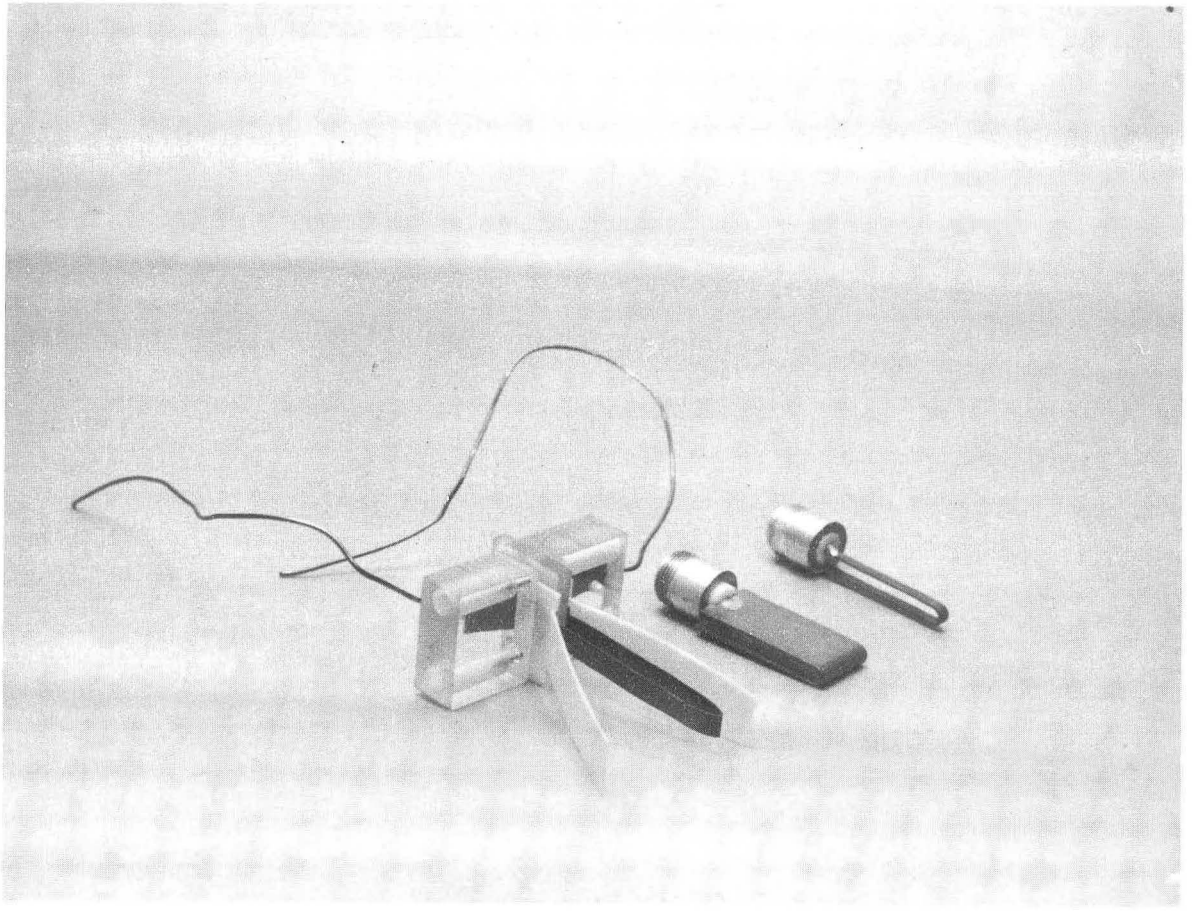

ZN-2385

Fig. 13. Strap hairpins.

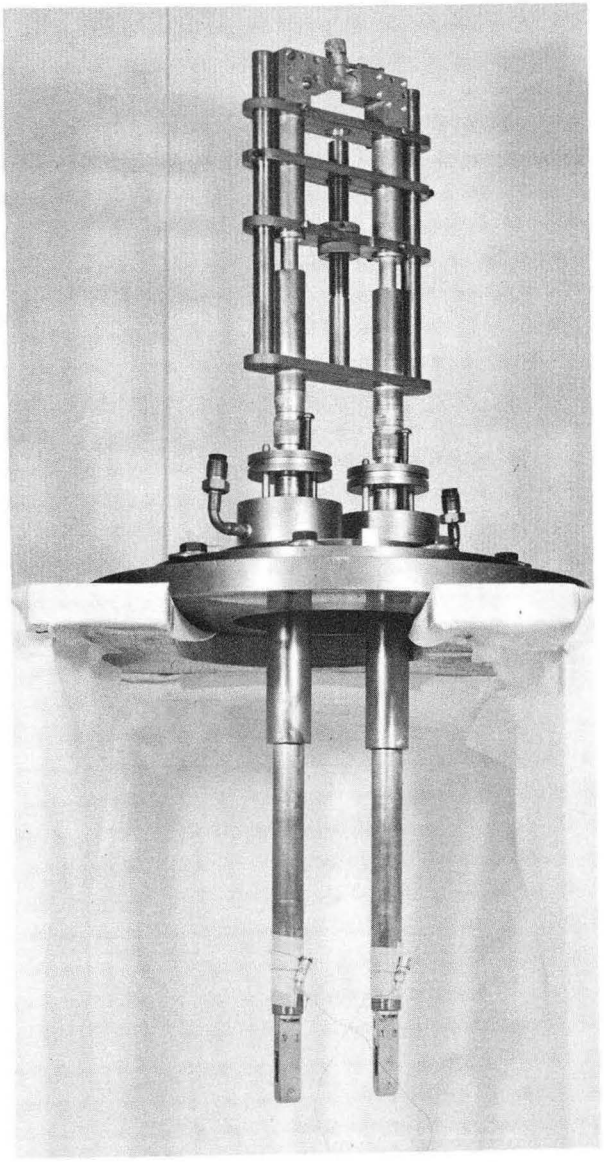

ZN-3813

Fig. 14. Ramsey hairpin.

effort was made to identify such a pattern. This study was made by using Cs^{133} at a field-independent point of $H_0 = 1250$ G and $\nu \approx 8500$ Mc/sec. No pattern was identified, yet there was considerable structure on the resonance. This could be traced to each individual hairpin rather than to an interference between the two hairpins. It was felt that the electromagnetic field structure within the hairpin was both uneven and unpredictable. The hairpin was abandoned and emphasis was shifted to the construction of a waveguide hairpin to be used with atomic-beam machine VI.

The velocity distribution of the atoms in the oven is Maxwellian. As a result, there are atoms emerging from the oven with very fast velocities and, therefore, they will suffer little deflection. This will add to the background of the resonances collected at the detector. These fast atoms may be removed from the beam by putting in a stopwire to block geometrically the optical path from the oven to the detector. This stopwire was placed in the B magnet (Fig. 9).

B. Atomic-Beam Machine VI and High-Frequency Equipment

As was discussed earlier, a second atomic-beam machine was used. A C magnet with a large gap between the poles was needed in order to use a section of x-band waveguide as a hairpin. This machine will now be described.

The layout is again like that shown in Fig. 9, and likewise is a flop-in type of machine. Figures 15(a) and 15(b) shown external pictures of this machine; a console area for the operation of the machine can be seen in Fig. 16. This area includes all operational instrumentation except the rf equipment. Again, oil diffusion pumps are used—a total of eight. Four of them pump on the main can: one each on the detector, the buffer, and the oven chambers; and an intermediate pump between the machanical pump and the main-can pumps.

One of the features of this machine is that the oven chamber, the buffer chamber, and the main can can be isolated from each other by large gate valves. Within each of the oven and buffer chambers there

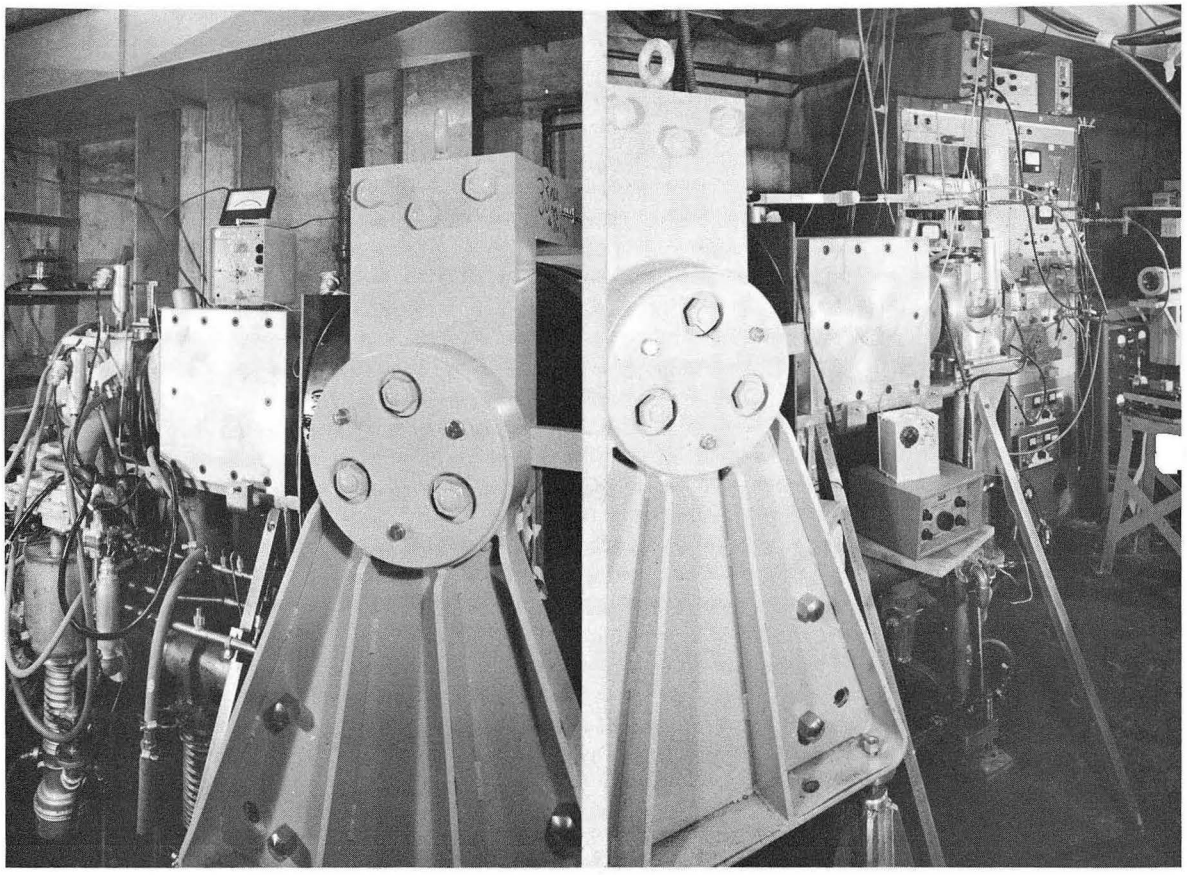

(a) (b)

ZN-3814

Fig. 15 (a). Atomic-beam machine VI (oven end).

Fig. 15(b). Atomic-beam machine VI (detector end).

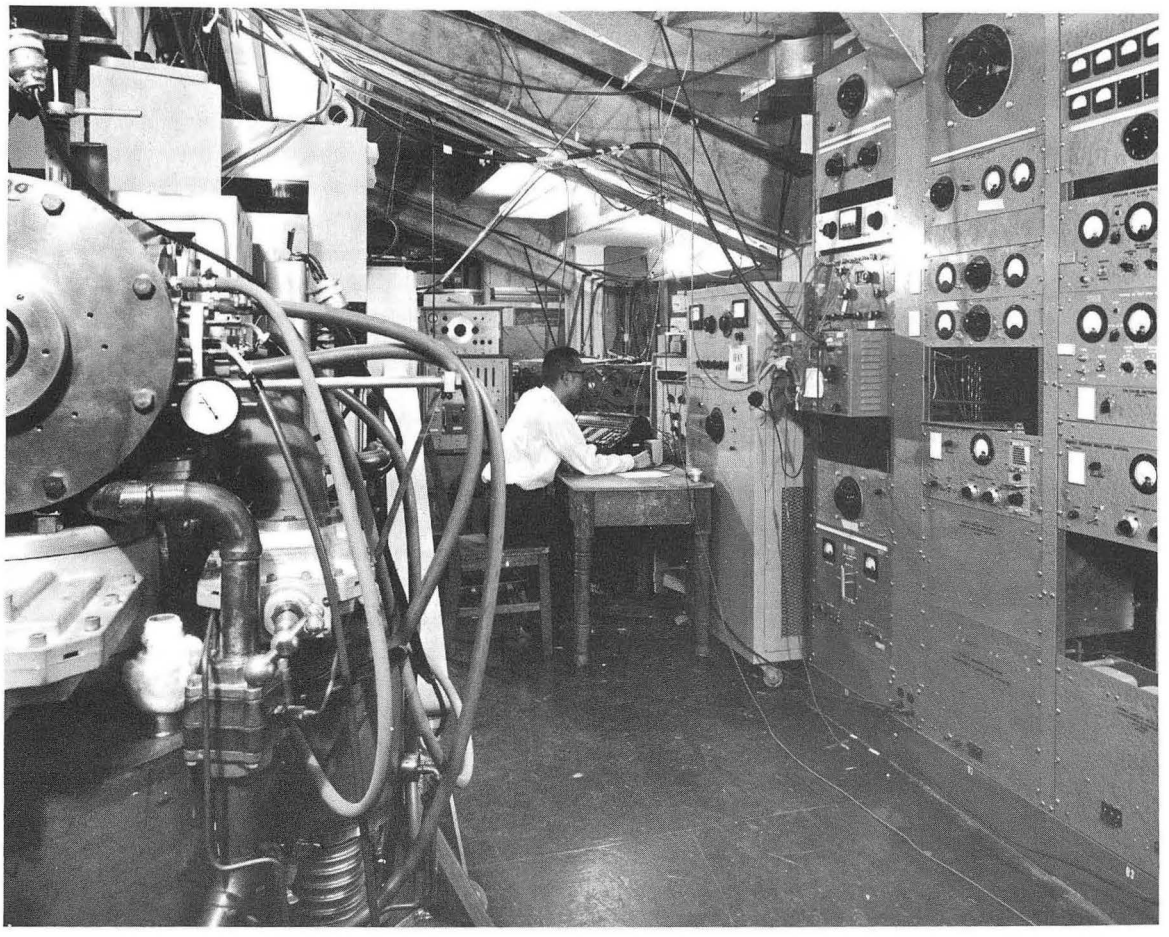

ZN-3810

Fig. 16. Console area.

is another gate valve by which the diffusion pump itself can be isolated from its respective chamber. The buffer chamber and the oven chamber may then be raised individually to atmospheric pressure even if their respective diffusion pumps are on. This is a very useful arrangement and permits quick entry into the system.

The ovens are introduced into the oven chamber by way of a side-loader through pumpouts. Hydraulic control is used in moving the oven platform in and out of the oven chamber. Pressure in this chamber is about 3×10^{-6} mm Hg. The buffer chamber is equipped with a resistance-heated oven, and the present arrangement does not allow both beams to be operating at the same time. Because of the method of heating, this oven is restricted to fairly low temperatures, easily within the range of the metal alkalis. The oven chamber heat source is from electron bombardment as described for atomic beam machine I.

Another feature of the machine is the small main-can volume. This is accomplished by keeping the three magnets outside of the evacuated chamber; as a result there is an increase in pumping speed. The pressure in the main can is about 1×10^{-7} mm Hg.

The three magnets still have the same basic shape as their counterpart on the machine already discussed, but each now is a high-impedance magnet with voltage regulation. The value of the A and B fields is approximately 8000 G at the beam position. The C field is generated by The Varian Associates V4012A 12-in. magnet and the magnet-regulated voltage supply, model V2100. This magnet has 12-in.-diam pole tips and a gap width of 1-3/4 in. The regulated supply provides 1 part in 10^5 regulation. Twenty-four hours before the run, all three magnets are turned on and set at the value for the experiment and are allowed to stabilize. This reduces the drift to negligible proportions.

There is only one hot-wire detector, and a similar radioactive detector as in the other machine. The buttons for this machine are longer than those of the other machine; this gives increased collecting area. To increase the signal-to-noise ratio (at the time of the experiment the machine did not have a stopwire), the width of the button was decreased from about 200 mils to about 100 mils. This choice was

based on Cs^{133} beam-profile considerations in which the resonance profile was compared with the zero-rf profile.

The rf circuit must be changed slightly in order to reduce the sidebands as much as possible in the hairpin. It is still desirable to lock an oscillator to the crystal, and it has been the policy in the past to multiply the frequencies many times rather than lock a klystron at the final frequency. The reason for this is that equipment was available for the multiplication process and difficulty was not really expected at the beginning. Two typical high-frequency circuits are given in Figs. 17 and 18. Line widths of 10 to 20 kc/sec were expected at the field-independent point and rf frequency changes across these resonances would be in 2-1/2- to 5-kc/sec steps. Therefore, it is desirable to have the uncertainty of the generated frequency less than this.

The output frequency was examined just before it went into the hairpin. This frequency was examined in two different ways. The first approach was to beat this frequency with a harmonic frequency from a free-running oscillator, and to observe the beat frequency. The Hewlett-Packard transfer oscillator model 540B was used. All impurities were attributed to the input signal. A second way was to multiply another very stable but fixed-frequency oscillator and beat this with the signal in question. If the beat frequency is say 10 kc/sec, it may be viewed on an oscilloscope and the frequency deviation of the signal may be estimated. The General Radio Co. frequency units (models 1112A and 1112B) were used as the reference in which the residual frequency modulation is less than one part in 10^9. The result was that the frequency-generation procedure of Fig. 17 gave rise to about 10 kc/sec frequency modulation deviation. In this case, the low-frequency oscillator (AM-1) was multiplied about 40 times. In Fig. 18 the resulting deviation was about 2 or 3 kc/sec, and the low frequency oscillator was multiplied only about 4 times. The frequency modulation was originating in either the AM-1 or FM-4 low-frequency oscillator. It is believed that the deviation arises from the phase-lock process of these two units.

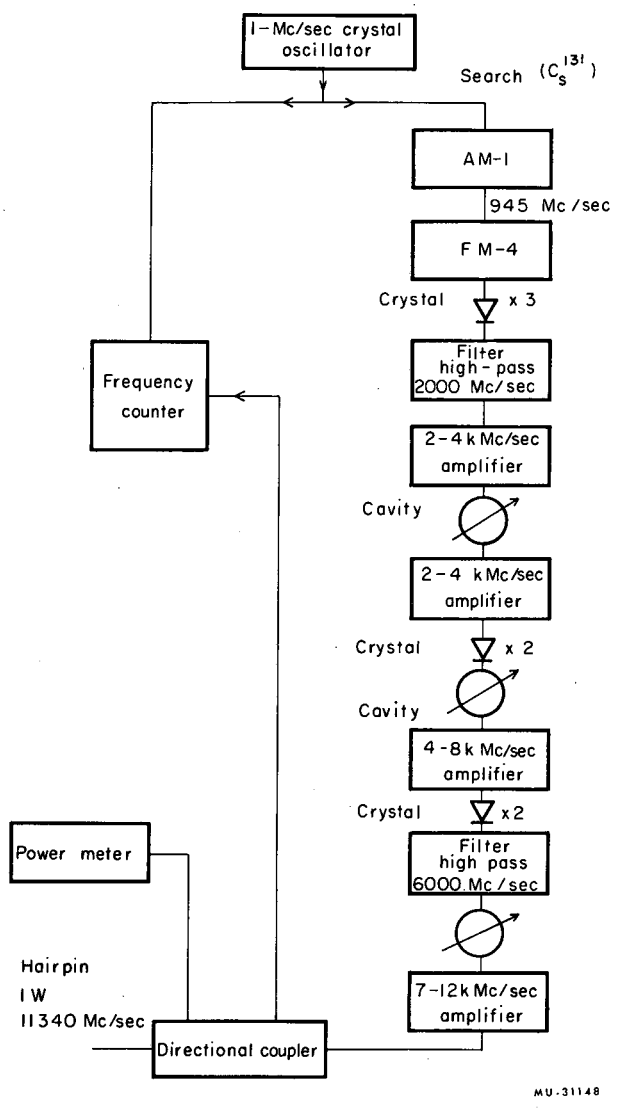

Fig. 17. Electronic circuit (high frequency).

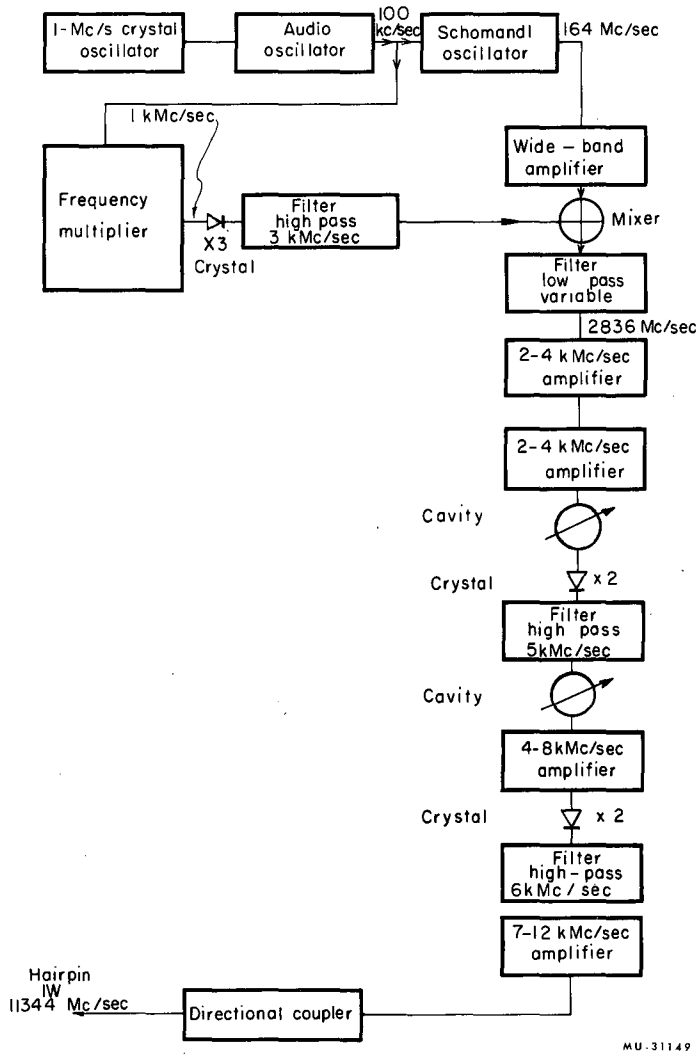

Fig. 18. Electronic circuit (high frequency).

Care must be taken, too, when multiplying frequencies, in that not only is the deviation multiplied, but the amplitude of the central frequency relative to the amplitude of the side bands will be altered. This can be seen as follows. Let the voltage oscillation be cos $\phi(t)$, where

$$\phi(t) = \omega_0 t + \delta \sin \omega_m t,$$

and ω_0 is the central frequency, δ is the deviation, and ω_m is the frequency of modulation. For small δ an expansion of cos $\phi(t)$ in a Bessel series produces the contributions of the carrier plus the sidebands with the carrier amplitude large relative to the sideband amplitude. Barnes and Mockler (BAR 60) showed that the effect of multiplication (N times) may be

$$\cos N\phi(t) = \cos (N\omega_0 t + N\delta \sin \omega_m t),$$

which, when expanded, has a different amplitude distribution between carrier and sidebands. A particular case can arise when the carrier amplitude reaches zero and all the power is in the sidebands. The above reference cites experimental evidence of this. For example, it was shown that multiplication by a factor of 9 was sufficient to reduce the carrier amplitude to about zero. The net result is a broadening of the power spectrum of the output frequency. Barnes and Mockler also showed that if there are two modulation frequencies the result of multiplication may be one which is not even symmetrical about the carrier frequency. As mentioned above, the output frequency was in error by only 2 or 3 kc/sec, and this was sufficient for the experiment. The above shift in the power spectrum (due to several modulation frequencies) could not be detected within this 2- or 3-kc/sec range. Figure 19 shows the electronics used to produce the frequencies.

A shielded strap hairpin and a waveguide hairpin were used (Fig. 20). The strap hairpin was used for the low-frequency calibration ($\approx$ 2 kMc/sec), and the waveguide hairpin was used for the sweep frequency ($\approx$ 12 kMc/sec). They both were mounted rigidly on a movable plate so that each hairpin could be placed at the same space point along

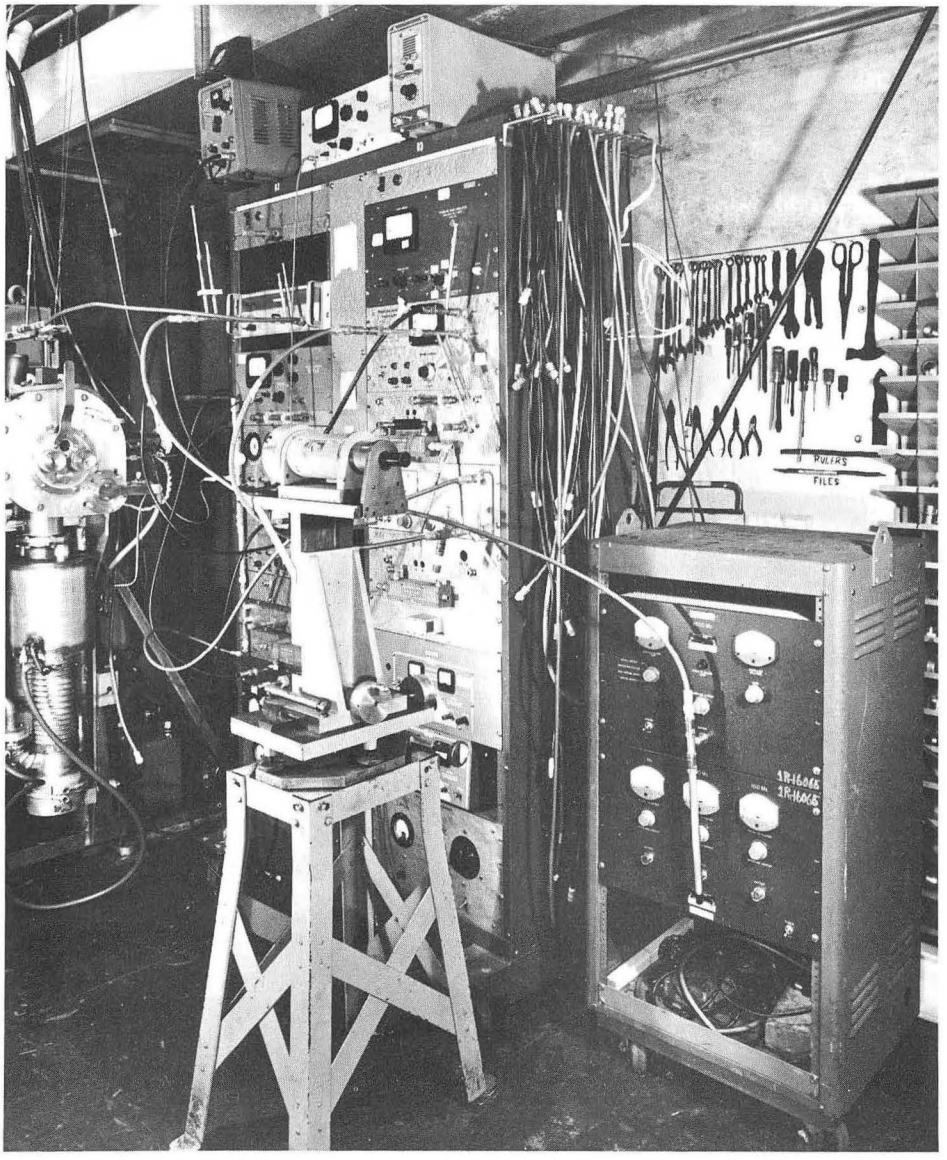

ZN-3811

Fig. 19. Electronics.

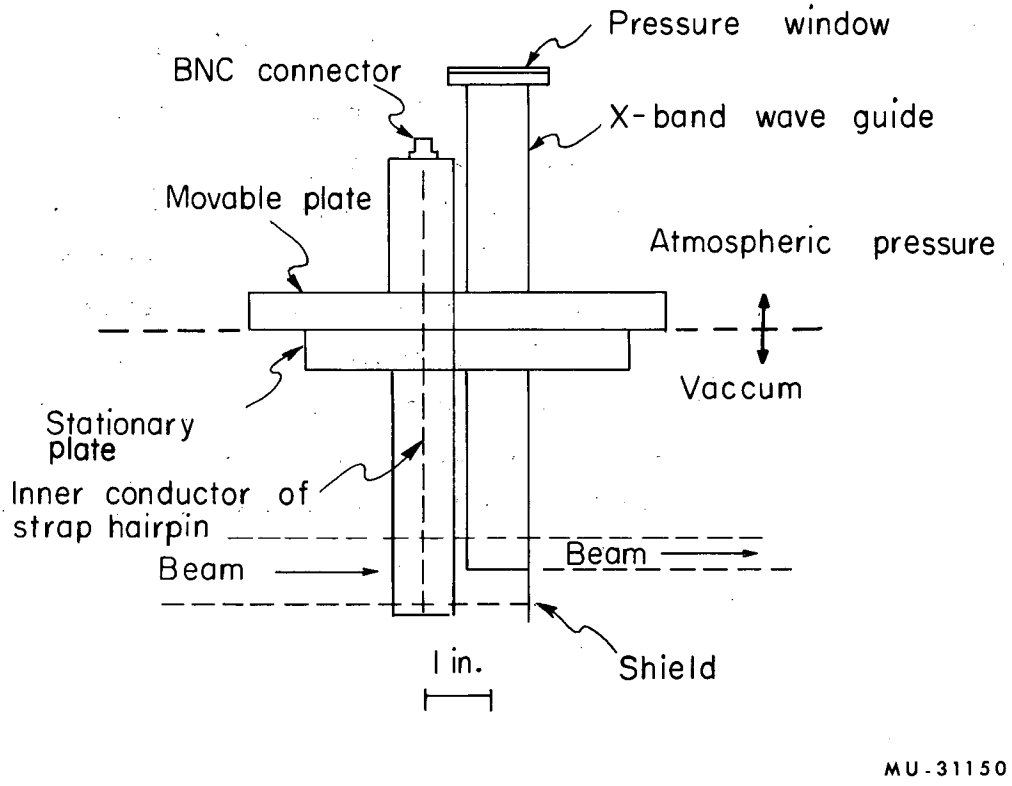

Fig. 20. Strap and waveguide hairpin assembly.

the beam. This was necessary for the calibration since there is always a slight variation of magnetic field in the magnet. The waveguide electromagnetic field mode was H_{01}, therefore the magnetic field would be parallel to the beam. Figure 21 shows the hairpins in place within the C magnet.

C. Radiation Detection

Cesium-131 decays by electron capture to Xe^{131}, which yields a K-shell x ray of about 35 keV and internal bremsstrahlung radiation. The x ray is easily detected by a thallium-activated NaI crystal (approximately 2 mm thick). The scintillation-counter head and button are shown in Fig. 11. The ball bearing locks the button to a fixed position, thus reproducing the same geometry for each button, and the crystal is shielded within a thick lead pig. The output from the photomultiplier tube is fed into a single-channel pulse-height analyzer and scalar. Four separate counting units are used to count the buttons to increase the counting statistics.

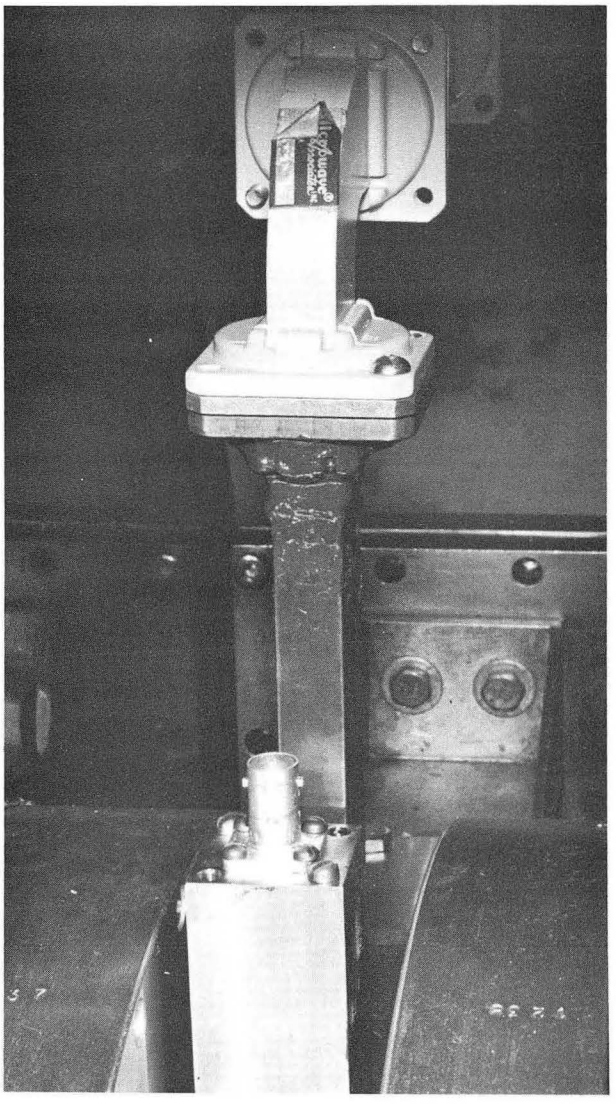

ZN-3812

Fig. 21. Strap and waveguide hairpin in C-magnet.

VI. RESULTS

In this section the experimental results are discussed and the theoretical values predicted for Cs^{131} are given. The discussion of the experimental results will include a brief examination of the low-frequency contribution, a rather detailed analysis of the high-frequency resonances, and, lastly, the final values of $\Delta\nu$ and g_I. Justification of the final value will be given as will also the calculation of the anomaly that is to be predicted by theory. Next, the theoretical predictions of the anomaly, Δ, and the magnetic moment, μ_I, will be given in detail.

A. Experimental Results

1. Analysis of the Low-Frequency Measurement

Of the 20 resonances, 8 were $\Delta F = 0$ transitions. Figures 22 through 25 show typical resonances as the magnetic field is increased. The lines broaden as the field is increased; in general the lines were symmetrical. In the final consistency check performed on the computer (discussed in Sec. IV), the frequency error attached to these resonances ranged from one-quarter to one-half of the full width at half maximum, depending on the shape of the line. In general this is considered a conservative value for the error. The $\Delta F = 0$ transition searches were terminated when $\delta(\Delta\nu) = \pm 4$ Mc/sec.

2. Analysis of the High-Frequency Measurement

From Eq. (II. 14), it is seen that at low fields the doublet is not resolved, but it should be resolved at some higher field. The first experiment was run at the lowest possible field, 636 G (see Sec. IV). Figure 26 shows the doublet is not resolved. The next experiment was at 1500 G and the doublet was clearly resolved (Fig. 27). The correct separation of about 3 Mc/sec was observed. The field-independent point was reached by using a 1/4-in. strap hairpin, resulting in 60- to 80-kc/sec linewidths. It was at this point that the switch from machine I to machine VI was made and a shorted waveguide was used for the hairpin. At first difficulty was encountered with the power spectrum of

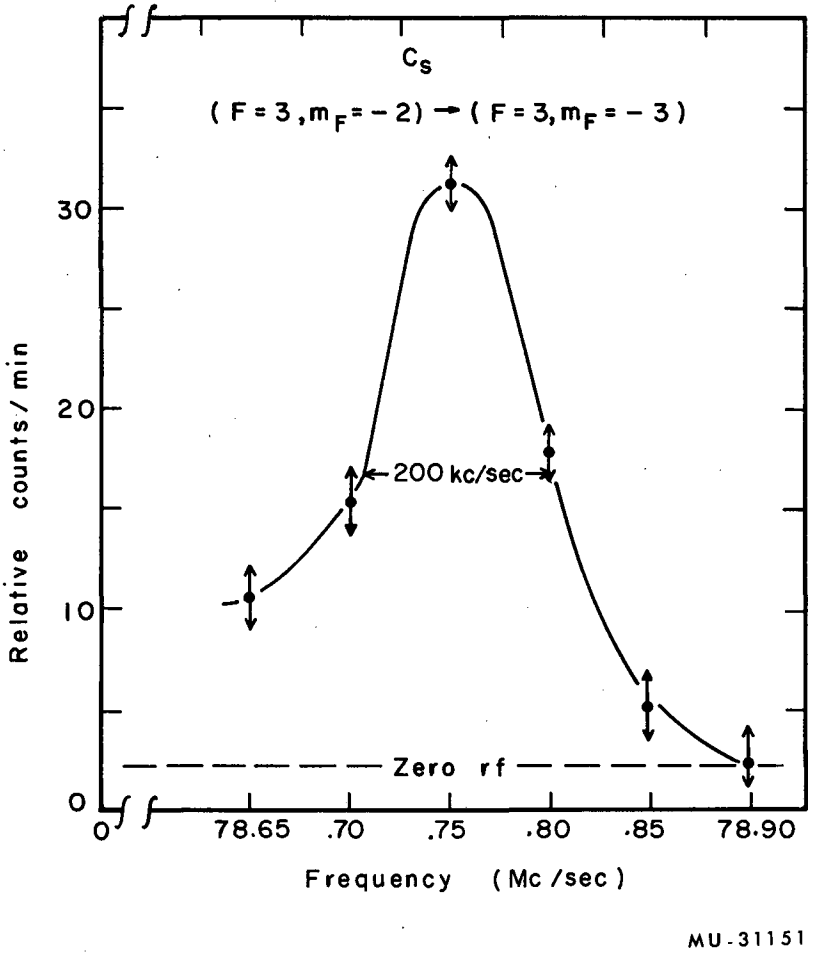

Fig. 22. $\Delta F = 0$ transition at 163.923 (83) G.

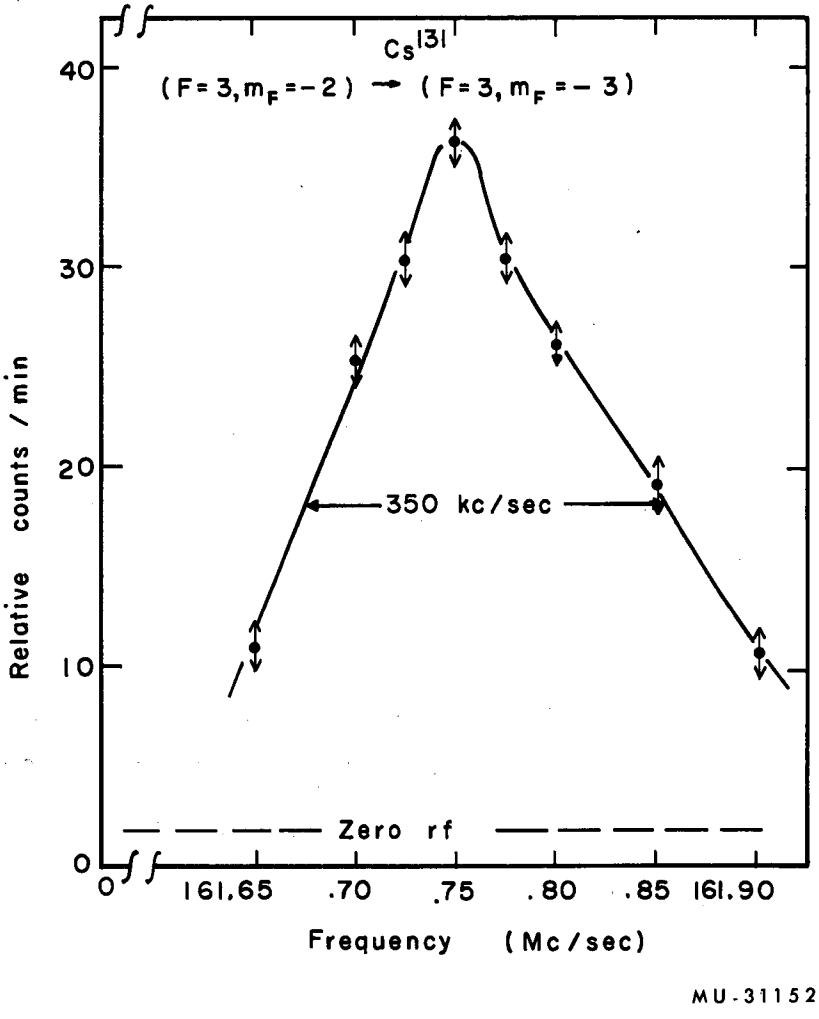

Fig. 23. $\Delta F = 0$ transition at 327.005 (64) G.

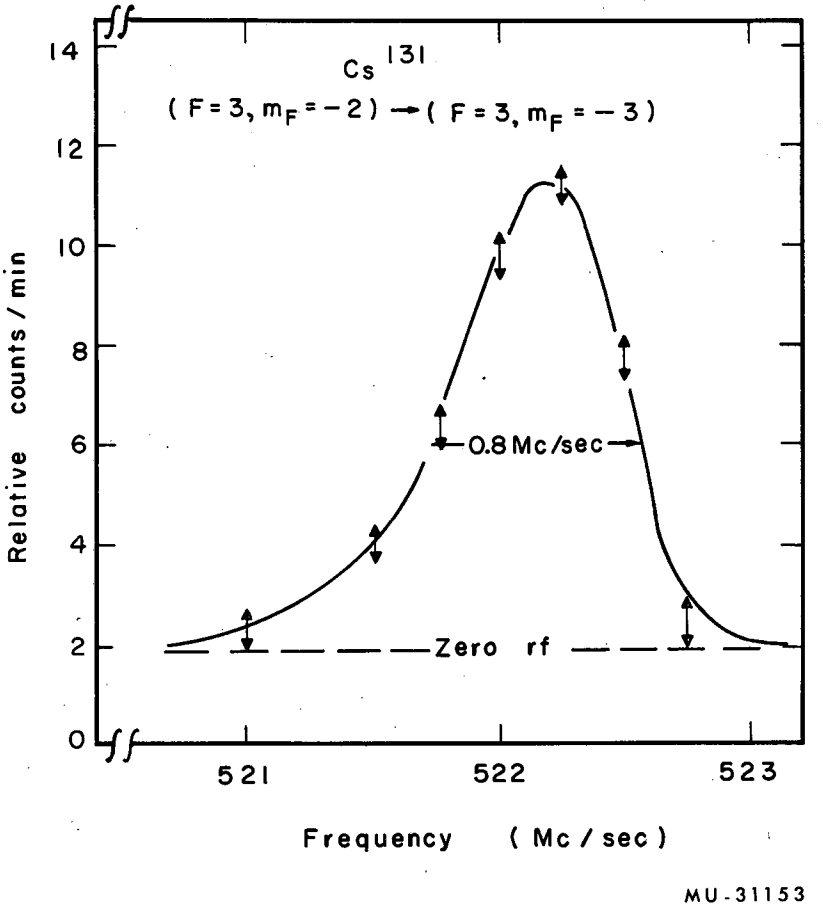

Fig. 24. $\Delta F = 0$ transition at 939.949 (66) G.

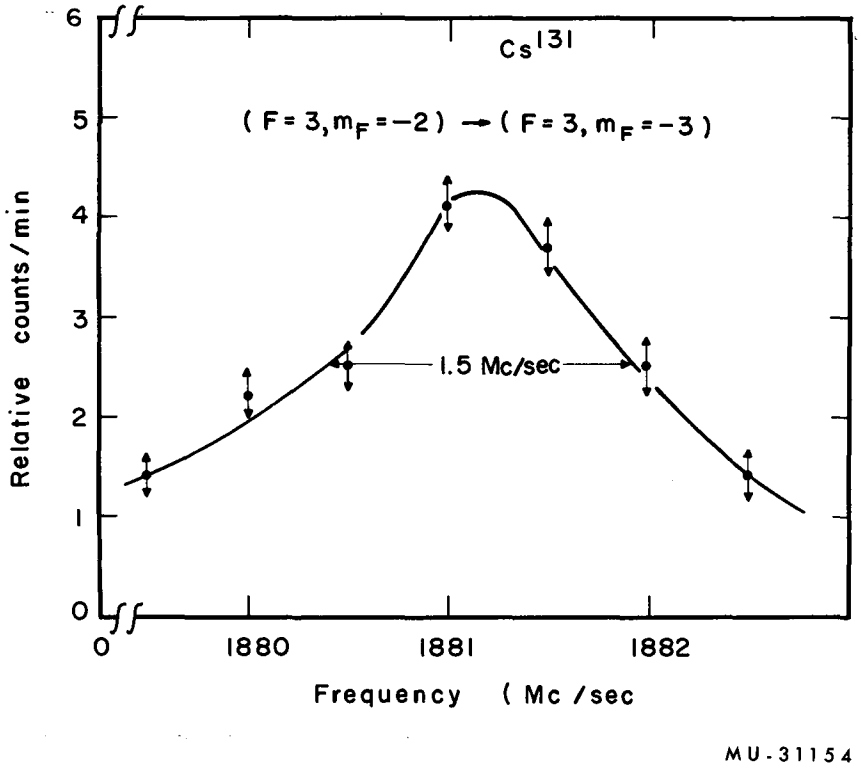

Fig. 25. $\Delta F = 0$ transition at 2480.25 (57) G.

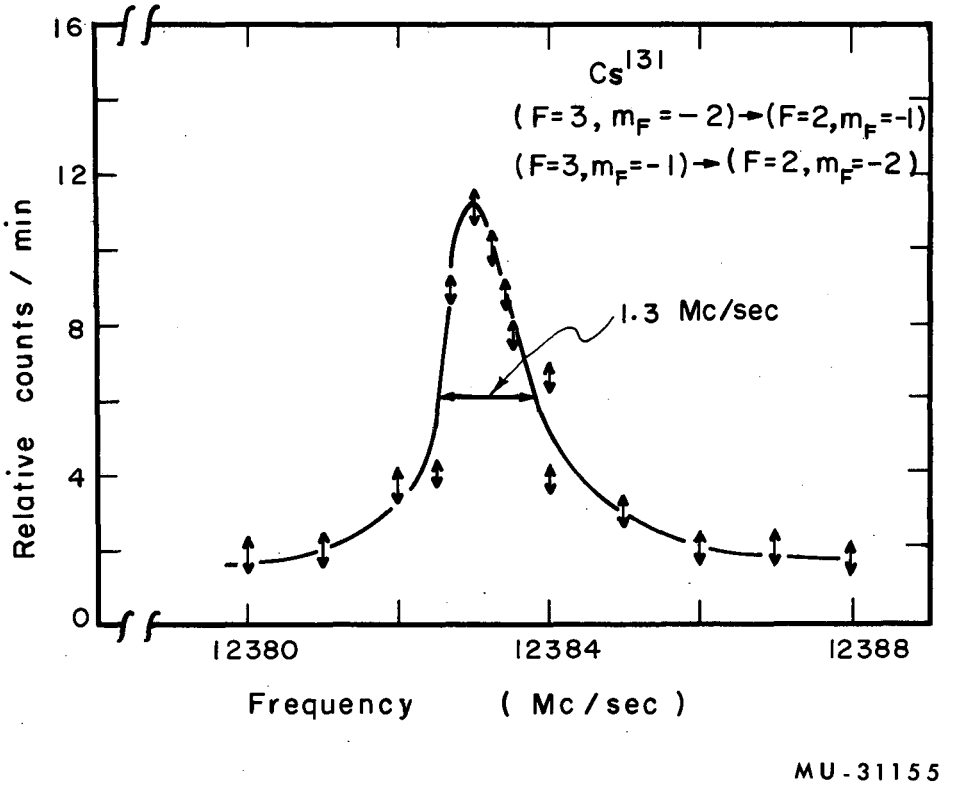

Fig. 26. Unresolved doublet at 635.704(96) G.

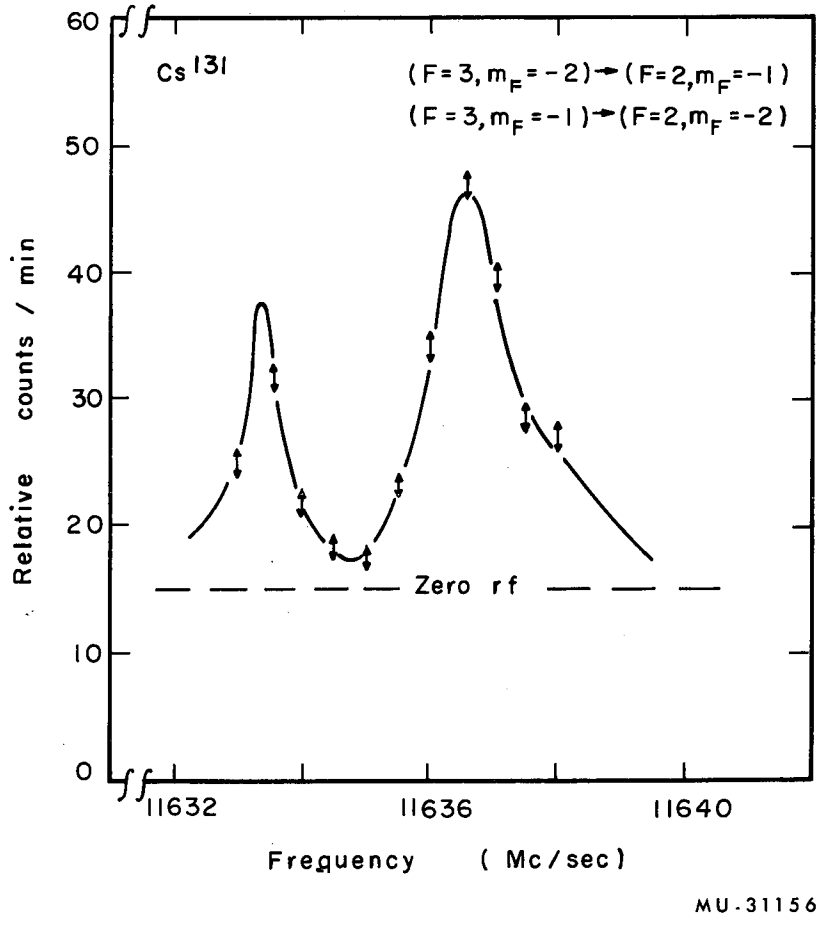

Fig. 27. Resolved doublet at 1499.45(18) G.

the rf. Resonances of Figs. 28 and 29 show a broad spectrum of frequencies in the hairpin. The spectrum is also power-dependent since Figs. 29 and 30 are the same doublet component at different powers. A great deal of care must be taken in generating the high frequencies. Figures 29 and 30 show signs of structure appearing at lower powers. This structure is also present in the other doublet component. Considerable attention was given to the investigation of this line shape. The analysis now follows.

The field-independent doublet of Cs^{133} at 1250 G was examined extensively with the waveguide hairpin. In all cases at lower powers each of the doublet frequencies was split into two lines just as was encountered for Cs^{131}. The procedure was to calibrate by using the low-frequency hairpin, then to sweep the high-frequency doublet of Cs^{133} by slowly varying the low-frequency oscillator by using a 1 rpm motor and feeding the output of the detector through an electrometer to a recorder. A typical trace has been reproduced in Fig. 31. After the trace was made the values of each peak and the trough were accurately taken by using the Hewlett-Packard transfer oscillator and a frequency counter. The estimated errors of Fig. 31 are ± 1 kc/sec in the frequency and ± 0.02 G in the field. The actual frequency is known to a few cycles per second. The following table gives typical values of the two peaks and the trough.

	Peak 1	Trough	Peak 2	Average	Predicted frequency
Doublet I					
(4, -2)→(3, -1)	8509.5244	8509.5304	8509.5492	8509.5368 ± 0.002	8509.5369 ± 0.0001
Doublet II					
(4, -1)→(3, -2)	8508.1272	8508.1404	8508.1512	8508.1392 ± 0.002	8508.1406 ± 0.0001

All frequencies are in Mc/sec; the average value in the table is the average of the two peak values. The two peaks were separated by about

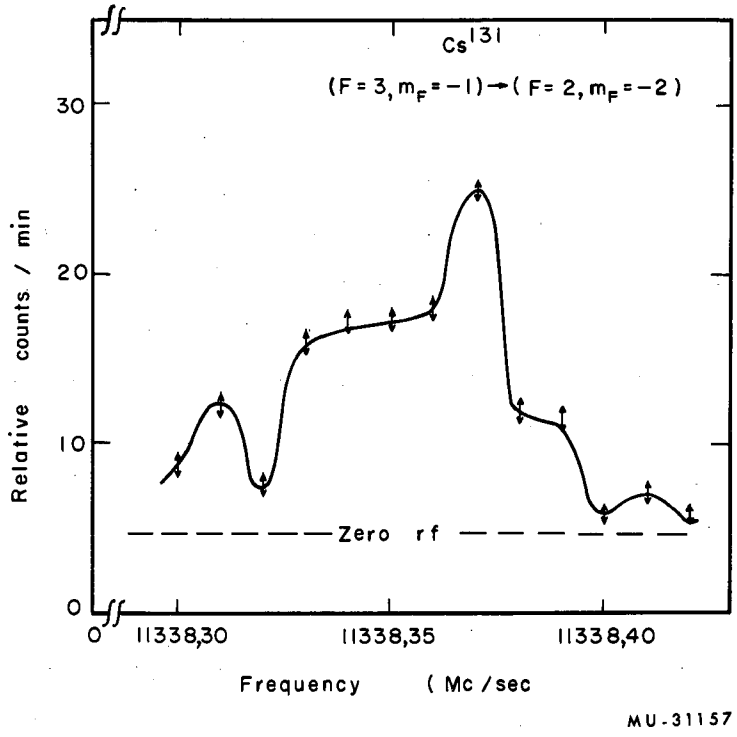

Fig. 28. Field-independent transition at 2443.656 (36) G.

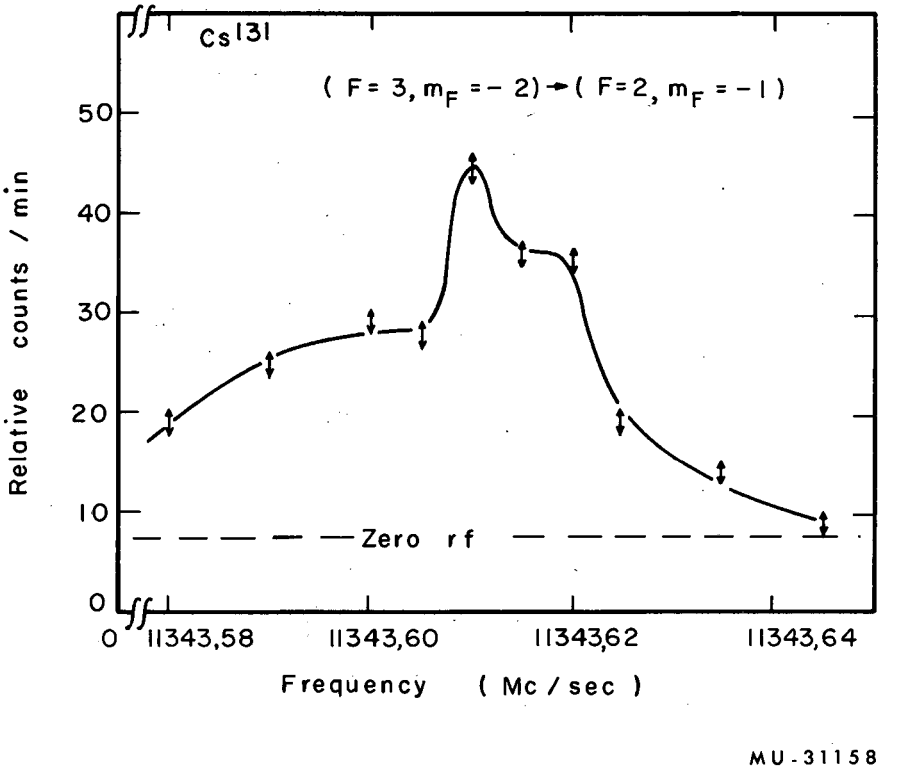

Fig. 29. Field-independent transition at 2440.506 (36) G

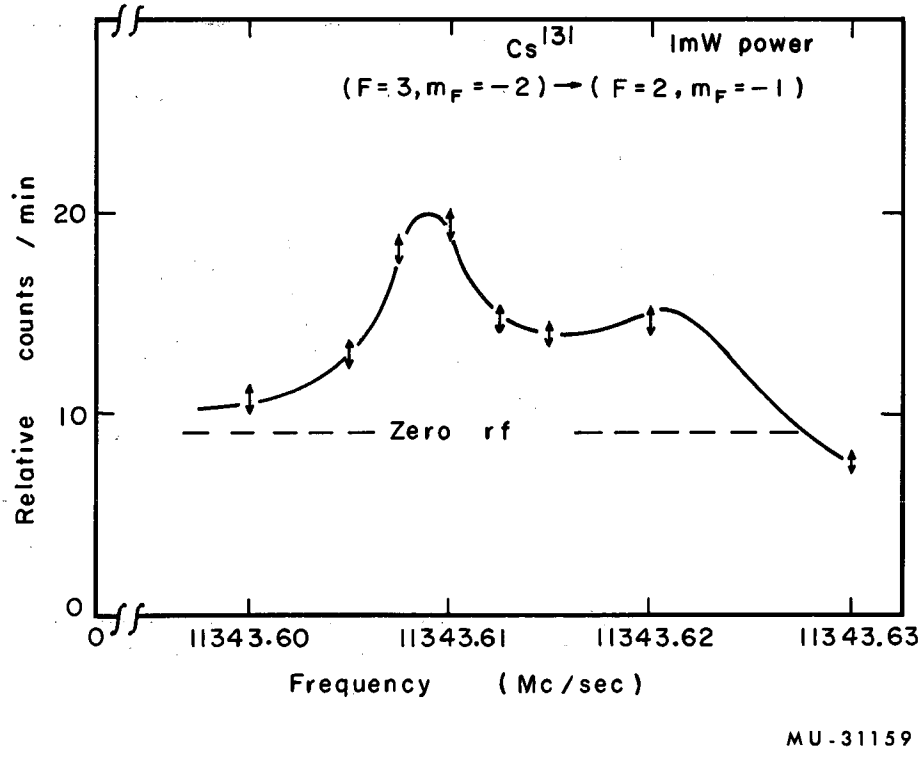

Fig. 30. Field-independent transition at 2440.506 (36) G.

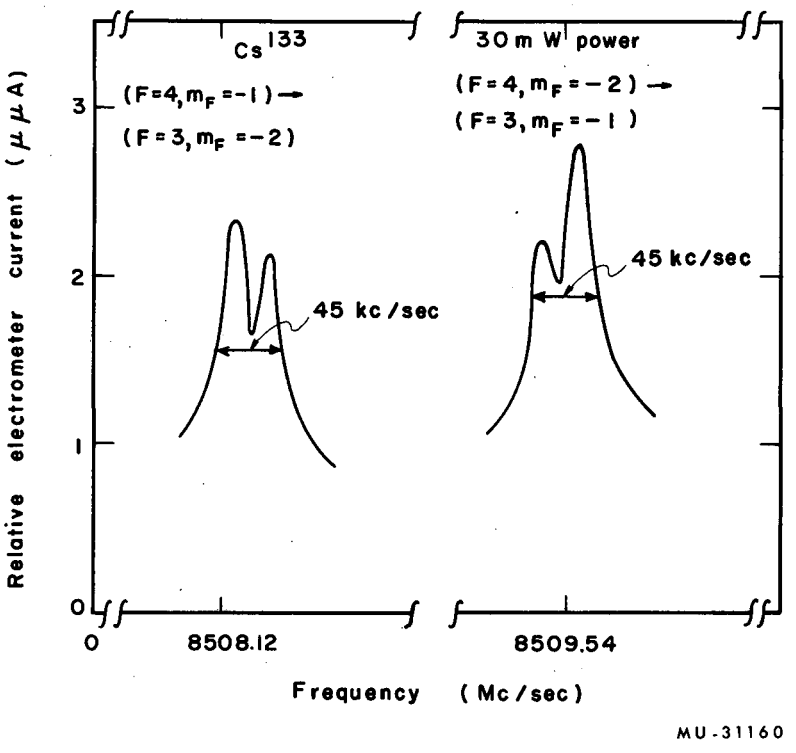

Fig. 31. Cs^{133} field-independent doublet at 1250.00(2) G.

24 kc/sec. It is clear that neither peak is the frequency and that the average of the two peaks does correspond to the frequency. The separation of the two peaks did not depend on power; however, for powers exceeding 200 mW the peaks overlapped to form only one resonance as shown in Fig. 32.

Since the beam hole was at the bottom of the hairpin at the short (see Fig. 20), the Millman effect (MIL 39) might be appreciable. However, this can only shift the frequency and cannot be the cause of the split in the frequency. In order to reduce the Millman effect, the beam hole was raised and centered about the point $\lambda/4$ from the short and the height of the beam hole was 5/32 in. This is only about $\lambda/8$ and therefore the field lines should be fairly straight at the beam position. Figure 33 shows the results — the split is even more pronounced. The rf used for this resonance was also very clean, with only about 2 kc/sec frequency modulation deviation.

The above shift can be explained by the Doppler effect. Barlow (BAR49), in discussing mode propagation in rectangular waveguides, develops the H_{01} mode by superimposing two composite waves making an angle γ with the waveguide axis, in which

$$\cos \gamma = \frac{\lambda}{\lambda_g},$$

where λ is the wavelength in free space and λ_g is the waveguide wavelength (λ_g is calculated in terms of the cutoff wavelength of the guide). Since the beam is incident at right angles to the waveguide axis, the Doppler effect predicts a splitting of

$$\delta\nu = \pm \nu \frac{v_B}{c} \sin \gamma,$$

where c is the velocity of light and v_B is the average beam velocity of the atoms. By using 350°C for the oven temperature, the calculated separation for Cs^{133} and Cs^{131} is 16.5 kc/sec, as compared with the 24 kc/sec measured. The difference may be attributed to the behavior of the transition probability for a velocity-dependent frequency as above. Since the frequency now depends on velocity, the average over the beam

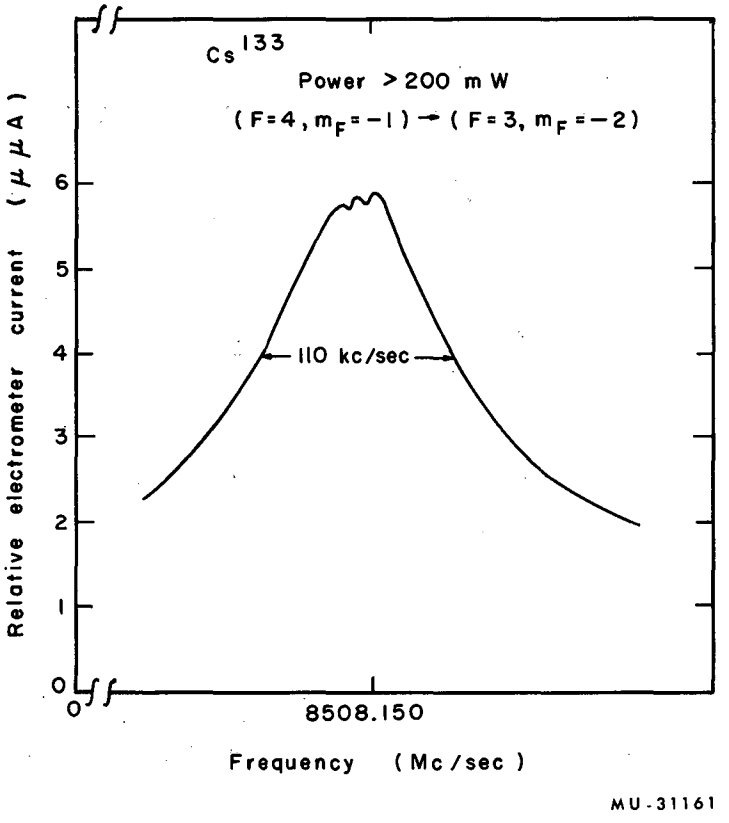

Fig. 32. Cs^{133} field-independent doublet at 1250.00(2) G.

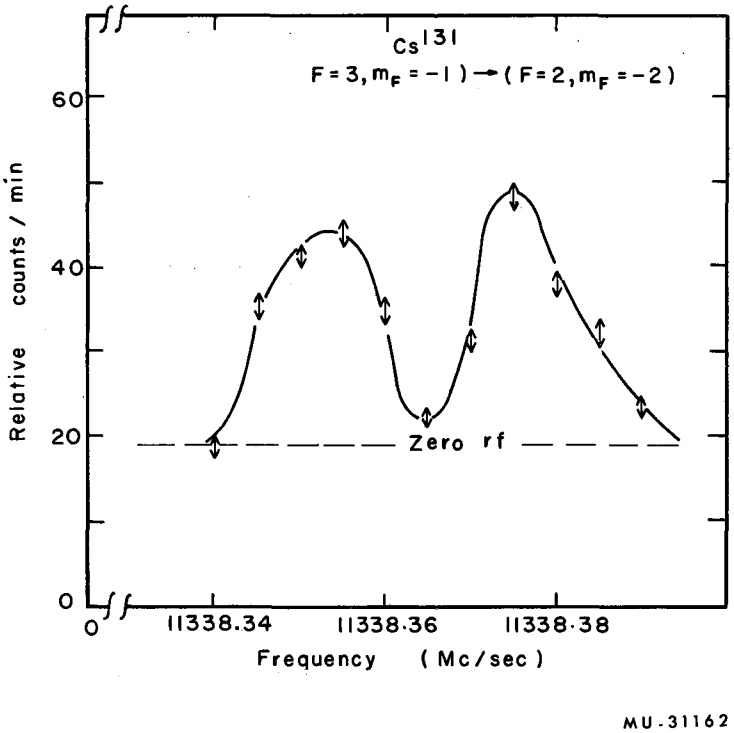

Fig. 33. field-independent transition at 2443.665(36) G.

velocity is not as straightforward as in previous cases. The larger the velocity, the larger the splitting, and one would expect the transition probability to be broadened on the side of the resonance that is farther away from the central minimum. This would then give rise to a larger measured splitting than that calculated above. The cause of the unequal heights of the Doppler components of Fig. 31 is not well understood. It is probably due to a combination of an uneven power distribution within the guide and an averaging over the beam velocities. The asymmetry was also detected slightly in the radioactive resonances of Figs. 30 and 33.

The two composite waves mentioned by Barlow (BAR49) will intercept the beam at right angles if the beam were allowed to enter the broad face of the guide. Therefore, as a final check of the existence of the Doppler effect, the guide was twisted 90 deg and again Cs^{133} was examined. There is little power in the center of the guide; therefore, the beam entered slightly off center of this face. Unfortunately, the bend was not made well and because of poor power distribution within the hairpin, structure resulted on top of the resonance. However, in all cases the central peak corresponded to the expected frequency, and the linewidth corresponded to the 1/2-in. dimension of the waveguide ($\approx$ 40 kc/sec), indicating that only one resonance was there. No radioactive resonances were measured by using this modified hairpin.

From the above analysis, the following interpretation of the data will be used. If two peaks occur, then the resonant frequency will be the average of the two peaks. If one resonance occurs (higher power) the resonant frequency is the frequency of the central peak. This interpretation gave very consistent results as tested by the computer routine discussed in Sec. IV.

3. Final Values of $\Delta\nu$ and μ_I

The final values of $\Delta\nu$ and μ_I are obtained after considering all the data. Each resonance was weighted according to the reciprocal of its line width and the computer calculated a "best fit value" of $\Delta\nu$ and μ_I and a probable error. The field-independent resonances are the

narrowest and therefore receive the most weight, but the final value of $\Delta\nu$ and μ_I do represent the entire collection of data and not just a single experiment. The best-fit values for Cs^{131} are

$$\Delta\nu = 13181.3805(30) \text{ Mc/sec},$$

$$g_I = 7.678(8) \times 10^{-4} \text{ (uncorrected)},$$

$$\mu_I = 3.525(4) \text{ nm} \quad \text{(uncorrected)}.$$

These values may be read directly from Fig. 35 which is the output from the HYPERFINE 3 machine calculation as discussed in Sec. IV. It must be remembered that $\Delta\nu = (I+1/2)a$. Also in the calculation there is an error of $(2)^{1/2}$ and the result is that the probable error in the printout must be multiplied by $(2)^{1/2}$. For the most part, Figs. 34 and 35 are self-explanatory. Figure 34 is a statement of the input data in which columns 3 and 4 list the calibration frequency and error for that particular run and columns 5 and 6 list the measured frequency and error for Cs^{131} for each run. Figure 35 summarizes the output where the final values of $\Delta\nu$ etc. are located in the upper portion of the printout. In the lower part of the printout the energy levels are listed in columns 3 and 4, and column 5 has the following meaning: Using the final values of $\Delta\nu$ etc. as calculated by the program, the measured frequency is calculated and compared with its measured value, and the difference is given in column 5. In all cases the difference is less than the experimental error. Column 13 lists the weight factor; "chi square" in the upper portion of the figure is a measure of the fit between the input and output data. The anomalies as calculated by Eq. (III. 3) are

$$^{131}\Delta^{133} = -0.65(10)\%,$$

$$^{131}\Delta^{135} = -0.61(10)\%.$$

B. Theoretical Predictions

1. Nuclear Magnetic Moment

As a first approximation one might expect that the net magnetic moment would be attributed to a single unpaired proton since the nucleus

ATOMIC BEAM RESEARCH ON RADIOACTIVE ATOMS
HYPERFINE 3
MAR. 26, 1963

ISOTOPE CS131

I= 5/2 J= 1/2

DATA FROM RUNS 179-194 TO FIT BEST VALUE OF A AND GI

COMPARING ISOTOPE

NAME	G_J	$G_I \times 10^4$	A	STATE
CS133	-2.002577	3.990120	2298.157959	S1/2

CALIBRATING ISOTOPES

NAME	I	G_J	$G_I \times 10^4$	DELTA U
RB85	5/2	-2.002409	2.937040	3035.7324
RB87	3/2	-2.002409	9.953590	6834.6826
CS133	7/2	-2.002577	3.990120	9192.6318
K39	3/2	-2.002309	1.419199	461.7197

OBSERVATIONAL INPUT DATA

	CALIBRATING ISOTOPE DATA			UNKNOWN ISOTOPE DATA							
RUN NO.	NAME	FREQ. (MC/SEC)	FREQ.ERROR (MC/SEC)	FREQ. (MC/SEC)	FREQ.ERROR (MC/SEC)	F 1	M 1	F 2	M 2	H (GAUSS)	DELTA H (GAUSS)
179	RB85	3.2600	0.0300	3.2500	0.0500	6/2	-4/2	6/2	-6/2	6.9467	0.0636
179	RB85	87.2180	0.0500	78.7500	0.0500	6/2	-4/2	6/2	-6/2	163.9233	0.0828
179	RB85	199.8500	0.0500	161.7500	0.0250	6/2	-4/2	6/2	-6/2	327.0052	0.0637
179	RB87	884.4100	0.0800	522.2000	0.4000	6/2	-4/2	6/2	-6/2	939.9493	0.0657
179	RB85	971.2700	0.1000	522.2000	0.3000	6/2	-4/2	6/2	-6/2	940.0903	0.0566
181	CS133	829.3800	0.1000	930.5000	0.5000	6/2	-4/2	6/2	-6/2	1499.5766	0.1199
181	CS133	1919.3300	0.8000	1881.2000	0.7500	6/2	-4/2	6/2	-6/2	2480.2475	0.5654
181	CS133	1918.8800	0.8000	1880.9000	0.7500	6/2	-4/2	6/2	-6/2	2479.9294	0.5655
182	RB85	510.6508	0.1200	12383.5000	1.0000	6/2	-4/2	4/2	-2/2	635.7044	0.0958
185	K39	3866.1000	0.5000	11636.7000	0.5000	6/2	-4/2	4/2	-2/2	1499.4549	0.1788
185	K39	3866.1000	0.5000	11633.5000	0.5000	6/2	-2/2	4/2	-4/2	1499.4549	0.1788
186	RB87	3421.0600	0.8500	11338.3829	0.0400	6/2	-2/2	4/2	-4/2	2440.7565	0.4041
186	RB87	3421.0600	0.8500	11343.6200	0.0250	6/2	-4/2	4/2	-2/2	2440.7565	0.4041
190	CS133	1867.9934	0.0500	11338.3700	0.0150	6/2	-2/2	4/2	-4/2	2443.6561	0.0359
190	CS133	1863.6145	0.0500	11343.6150	0.0100	6/2	-4/2	4/2	-2/2	2440.5060	0.0360
190	CS133	1863.6145	0.0500	11343.6200	0.0150	6/2	-4/2	4/2	-2/2	2440.5060	0.0360
190	CS133	1863.6145	0.0500	11343.6150	0.0100	6/2	-4/2	4/2	-2/2	2440.5060	0.0360
190	CS133	1863.6145	0.0500	11343.6139	0.0050	6/2	-4/2	4/2	-2/2	2440.5060	0.0360
194	CS133	1868.0060	0.0500	11338.3650	0.0050	6/2	-2/2	4/2	-4/2	2443.6651	0.0359
194	CS133	1863.6145	0.0500	11343.6150	0.0050	6/2	-4/2	4/2	-2/2	2440.5060	0.0360

NO. OF OBSERVATIONS = 20

MUB-1953

Fig. 34. Cs^{131} HYPERFINE 3 calculation.

MAGNETIC DIPOLE,ELECTRIC QUADRUPOLE AND G VARIABLES

CS131

ITERAT. NO.	A	$G_I \times 10^4$	ERROR IN A	ERROR IN $G_I \times 10^4$	CHI SQUARE
1	4393.8000	7.628627	0.	0.	0.51906607E 02
2	4393.7935	7.678407	0.0008	0.005819	0.10342322E 01
3	4393.7935	7.678429	0.0008	0.005819	0.10339314E 01

ENERGY LEVELS AND RESIDUALS

CS131

B = 0.
B/A = 0.
U/H = 1.399677
MP/ME= 1836.12
U_I = 3.524629

RUN NUMBER	FREQUENCY (MC/SEC)	ENERGY-1 (MC/SEC)	ENERGY-2 (MC/SEC)	RESIDUAL (MC/SEC)	FREQ ERROR (MC/SEC)	F 1	M 1	F 2	M 2	H (GAUSS)	DELTA H (GAUSS)	WEIGHT FACTOR
179	3.2500	5485.7678	5482.5248	0.0070	0.0500	6/2	-4/2	6/2	-6/2	6.9467	0.0636	295.2
179	78.7500	5341.6572	5262.9470	0.0397	0.0500	6/2	-4/2	6/2	-6/2	163.9233	0.0828	239.2
179	161.7500	5196.5829	5034.8290	-0.0038	0.0250	6/2	-4/2	6/2	-6/2	327.0052	0.0637	573.1
179	522.2000	4699.5495	4177.4468	0.0974	0.4000	6/2	-4/2	6/2	-6/2	939.9493	0.0657	6.2
179	522.2000	4699.4448	4177.2496	0.0048	0.3000	6/2	-4/2	6/2	-6/2	940.0903	0.0566	10.9
181	930.5000	4325.3015	3394.6437	-0.1578	0.5000	6/2	-4/2	6/2	-6/2	1499.5766	0.1199	3.9
181	1881.2000	3904.0463	2022.8875	0.0412	0.7500	6/2	-4/2	6/2	-6/2	2480.2475	0.5654	1.0
181	1880.9000	3904.1274	2023.3325	0.1050	0.7500	6/2	-4/2	6/2	-6/2	2479.9294	0.5655	1.0
182	12383.5000	4936.1141	-7447.2144	0.1715	1.0000	6/2	-4/2	4/2	-2/2	635.7044	0.0958	1.0
185	11636.7000	4325.3734	-7311.3197	0.0068	0.5000	6/2	-4/2	4/2	-2/2	1499.4549	0.1788	3.8
185	11633.5000	5117.6461	-6515.8240	0.0299	0.5000	6/2	-2/2	4/2	-4/2	1499.4549	0.1788	3.8
186	11338.3829	5237.5530	-6100.8152	0.0147	0.0400	6/2	-2/2	4/2	-4/2	2440.7565	0.4041	624.9
186	11343.6200	3914.4112	-7429.2035	0.0053	0.0250	6/2	-4/2	4/2	-2/2	2440.7565	0.4041	1599.7
190	11338.3700	5238.3438	-6100.0217	0.0045	0.0150	6/2	-2/2	4/2	-4/2	2443.6561	0.0359	4444.4
190	11343.6150	3914.4788	-7429.1359	0.0004	0.0100	6/2	-4/2	4/2	-2/2	2440.5060	0.0360	9999.9
190	11343.6200	3914.4788	-7429.1359	0.0054	0.0150	6/2	-4/2	4/2	-2/2	2440.5060	0.0360	4444.4
190	11343.6150	3914.4788	-7429.1359	0.0004	0.0100	6/2	-4/2	4/2	-2/2	2440.5060	0.0360	9999.9
190	11343.6139	3914.4788	-7429.1359	-0.0007	0.0050	6/2	-4/2	4/2	-2/2	2440.5060	0.0360	39997.7
194	11338.3650	5238.3463	-6100.0192	-0.0005	0.0050	6/2	-2/2	4/2	-4/2	2443.6651	0.0359	39997.6
194	11343.6150	3914.4788	-7429.1359	0.0004	0.0050	6/2	-4/2	4/2	-2/2	2440.5060	0.0360	39997.7

MUB-1954

Fig. 35. Cs^{131} HYPERFINE 3 calculation.

is composed of an odd-Z — odd-A combination ($Z = 55$, $N = 76$). The view here is that even numbers of nucleons give little contributions to macroscopic quantities. The single-particle value of μ_I, in nuclear magnetons, is given by the first two terms of Eq. (III.23),

$$\mu_I = a_S g_S + a_L g_L ,$$

for $I = 5/2$, $g_S = 5.585$, $g_L = 1$, then

$$\mu_I = 4.79 \text{ nm}.$$

This value is much too high and is indicative that the odd proton does not move in a spherical potential as required by the single-particle assumptions. As a correction to this value one might consider the collective model. This model presumes that nucleons other than the odd one form a nonspherical core around which the odd nucleon moves. The interaction of this nucleon with the deformed surface of the core results in a nuclear moment, as given by Bohr and Mottelson (BOH53),

$$\mu_I = \mu_{SP} - (g_I - g_R) \frac{I}{I+1},$$

where $I > 3/2$, μ_{SP} is the single-particle value of the moment, $g_R = Z/A \approx 0.41$, and g_I is given by Eq. (III.17). The value of the moment by using the collective model is

$$\mu_I = 3.71 \text{ nm}.$$

For the number of nucleons in the neighborhood of closed shells (closed shells are 50 and 82), the core deformation is not expected to be large. In support of this, the quadrupole moment of Cs^{133} is very small. It is therefore felt that the collective model for cesium would not be an adequate model.

The success of the Configuration Mixing Theory (CMT) in predicting the nuclear moments was stated in Sec. III. The procedure is to use Eq. (III.23) where the $a_0^{(i)}$ are related to the off-diagonal matrix elements for the moment between an admixed state and the ground state. These states differ by $\Delta L = 0$. The superscript i refers to the particular admixture. The ground state of Cs^{131} is not definite, but for the protons outside the closed shell, $Z = 50$ may be either $(2d_{5/2})^5$,

$(1g_{7/2})^4 2d_{5/2}$, $(1g_{7/2})^2(2d_{5/2})^3$, or some mixture of these. The neutrons are assumed to have the configuration for $N > 50$, $(1g_{7/2})^8 (2d_{5/2})^6 (1h_{11/2})^{12}$. To calculate the moment a ground state is assumed and all $\Delta L = 0$ excitations are considered provided they do not differ by more than one single particle state from the ground state; and, of course, they cannot be too far away in energy. The $a_0^{(i)}$ are calculated according to Stroke, Blin-Stoyle and Jaccarino (STR 61), and the moment is evaluated. The other two ground states are treated similarly. These ground states will be designated in Table VI, and the results of the calculation are tabulated for Cs^{131}, Cs^{133}, and Cs^{135} — since each of the moments is needed for the calculation of the anomaly. The particular excitations used for the calculation may be found in Table VII. Only those for which $\Delta L = 0$ may be used for the moment calculation; whereas, both a_0 and a_2 are used for the calculation of the anomaly.

For Cs^{131} the ground state appears to be a mixture of Cs_b^{131} and Cs_c^{131}; for Cs^{133}, a mixture of Cs_b^{133} and Cs_c^{133}; and for Cs^{135} the ground state lies close to Cs_c^{135}.

2. Hyperfine Structure Anomaly

The calculation of the anomaly (Eq. III.21) is much more involved. There is another quantity needed for the calculation besides $a_0^{(i)}$: excitations for which $\Delta L = 2$ will also contribute; these quantities are designated $a_2^{(i)}$ [see reference (STR 61)].

States Cs_b^{131}, Cs_c^{131}, Cs_b^{133}, Cs_c^{133}, and Cs_c^{135} from the moment calculation appear to be more promising than the others; and it is between these states that the anomaly will be reported. Table VIII summarizes these values along with the experimental values.

The calculated value of the anomaly $^{133}\Delta^{135}$ was included just to give a check for the calculation. As stated by Stroke, Blin-Stoyle and Jaccarino (STR 61), the errors in the calculation ($\approx 6\%$) result from estimating the electron wave function. These errors, unfortunately, produce an overlap of the anomalies for the various ground states assumed. The experimental value of the anomaly and the predicted value correspond well to within the estimated errors.

Table VI. Calculated moments.

Ground-state symbol	Ground state for neutrons (over 50)	Ground state for protons (over 50)	Nuclear moment μ_I (nm) (corrected)	Experimental value of μ_I (corrected)
Cs_a^{131}		$(2d_{5/2})^5$	2.65	
Cs_b^{131}	$(1g_{7/2})^8(2d_{5/2})^6(1h_{11/2})^{12}$	$2d_{5/2}(1g_{7/2})^4$	3.90	3.50
Cs_c^{131}		$(1g_{7/2})^2(2d_{5/2})^3$	3.27	
Cs_a^{133}		$(1g_{7/2})^5$	2.15	
Cs_b^{133}	$(1g_{7/2})^8(2d_{5/2})^6(3s_{1/2})^2(1h_{11/2})^{12}$	$(1g_{7/2})^3(2d_{5/2})^2$	2.47	2.55
Cs_c^{133}		$(1g_{7/2})(2d_{5/2})^4$	2.79	
Cs_a^{135}		$(1g_{7/2})^5$	2.09	
Cs_b^{135}	$(1g_{7/2})^8(2d_{5/2})^6(3s_{1/2})^2(1h_{11/2})^{12}(2d_{3/2})^2$	$(1g_{7/2})^3(2d_{5/2})^2$	2.41	2.71
Cs_c^{135}		$(1g_{7/2})(2d_{5/2})^4$	2.73	

Table VII. Excitations.

Isotope	Neutron excitations	Ground State	Proton excitations	ΔL	Type of excitation [see (STR61)]
Cs^{131}	$2d_{5/2} \rightarrow 2d_{3/2}$	Cs_a^{131}	$2d_{5/2} \rightarrow 1g_{7/2}$	2	III
	$1h_{9/2} \rightarrow 1h_{11/2}$		$2d_{5/2} \rightarrow 2d_{3/2}$	0	III
			$1g_{9/2} \rightarrow 1g_{7/2}$	0	I
		Cs_b^{131}	$1g_{9/2} \rightarrow 1g_{7/2}$	0	I
			$1g_{7/2} \rightarrow 2d_{5/2}$	2	II
			$2d_{5/2} \rightarrow 2d_{3/2}$	0	III
			$2d_{5/2} \rightarrow 1g_{7/2}$	2	III
		Cs_c^{131}	$1g_{9/2} \rightarrow 1g_{7/2}$	0	I
			$1g_{7/2} \rightarrow 2d_{5/2}$	2	II
			$2d_{5/2} \rightarrow 2d_{3/2}$	0	III
			$2d_{5/2} \rightarrow 1g_{7/2}$	2	III
Cs^{133}	$2d_{5/2} \rightarrow 2d_{3/2}$	Cs_a^{133}	$1g_{9/2} \rightarrow 1g_{7/2}$	0	II
	$1h_{11/2} \rightarrow 1h_{9/2}$		$1g_{7/2} \rightarrow 2d_{5/2}$	2	III
		Cs_b^{133}	$2d_{5/2} \rightarrow 2d_{3/2}$	0	I
			$1g_{9/2} \rightarrow 1g_{7/2}$	0	II
			$2d_{5/2} \rightarrow 1g_{7/2}$	2	II
			$1g_{7/2} \rightarrow 2d_{5/2}$	2	III
		Cs_c^{133}	$2d_{5/2} \rightarrow 2d_{3/2}$	0	I
			$1g_{9/2} \rightarrow 1g_{7/2}$	0	II
			$2d_{5/2} \rightarrow 1g_{7/2}$	2	II
			$1g_{7/2} \rightarrow 2d_{5/2}$	2	III
Cs^{135} (same as for Cs^{133})					

Table VIII. Theoretical and experimental results.

	Ground states	Theoretical anomaly (%)	Experimental value of anomaly (%)
$^{131}\Delta^{133}$	Cs_b^{131}-Cs_b^{133}	- 0.57(4)	- 0.65(10)
	Cs_c^{131}-Cs_c^{133}	- 0.53(4)	
	Cs_c^{131}-Cs_b^{133}	- 0.57(4)	
	Cs_b^{131}-Cs_c^{133}	- 0.53(4)	
$^{131}\Delta^{135}$	Cs_b^{131}-Cs_c^{135}	- 0.54(4)	- 0.61(10)
	Cs_c^{131}-Cs_c^{135}	- 0.54(4)	
$^{133}\Delta^{135}$	Cs_b^{133}-Cs_c^{135}	+ 0.030(8)	+ 0.037(9)
	Cs_c^{133}-Cs_c^{133}	- 0.010(8)	

It is of interest to quote the value of the anomaly if the corrections due to configuration mixing are deleted. This value is the same as would be obtained from Eq. (III.14). By using the measured value of the moment, the anomaly between Cs^{131} and Cs^{133} becomes - 0.94. This lies outside the experimental error. Thus the corrections due to CMT are in the right direction and agree nicely with experiment.

ACKNOWLEDGMENTS

I take great pleasure in thanking Professor William A. Nierenberg for his encouragement and support throughout this research.

Professor Howard A. Shugard contributed numerous helpful suggestions; I appreciate both his help and interest in the work.

There are many who contributed to the completion of this work. Especially, I wish to thank the following:

Dr. Vernon J. Ehlers and Dr. Y. W. Chan for contributing their knowledge and time during long hours of running.

Mr. Douglas Macdonald for his guidance in mechanical design and for expediting construction projects for me.

Frank Upham and Kenneth Lamers for the interest and help they have given me on the electronic problems.

The staff of the Health Chemistry Division of the Lawrence Radiation Laboratory for their assistance in handling the radioactive materials.

And above all, I wish to thank my wife, Joan, for her help and tolerance during this period.

This work was done under the auspices of the U. S. Atomic Energy Commission.

APPENDIX

The following is a list of numerical quantities useful for the calculations mentioned in the text.

$\Delta\nu(Cs^{133}) = 9192.63183(1)$ Mc/sec (ESS 55)

$\Delta\nu(Cs^{135}) = 9724.023(15)$ Mc/sec (STR 57)

$g_J(Cs) = -2.002577(27)$ (KUS 49)

$I(Cs^{133}) = 7/2$

$I(Cs^{135}) = 7/2$

$g_I(Cs^{133}) = 3.99012 \times 10^{-4}$ (uncorrected) (WAL 53)

$g_I(Cs^{135}) = 4.22234 \times 10^{-4}$ (STR 57)

The following list was taken from reference (COH 57):

$h = 6.62517(23) \times 10^{-27}$ erg-sec

$\mu_0 = 0.92731(2) \times 10^{-20}$ erg/G

$k = 1.38042(10) \times 10^{-16}$ erg/deg

$M_P/m_e = 1836.12(2)$

$\mu_N = \mu_0(m_e/M_P) = 0.505038(18) \times 10^{-23}$ erg/G.

REFERENCES

BAR 49: H. M. Barlow, Micro-Waves and Wave Guides (Dover Publications, New York, 1949).

BAR 60: J. A. Barnes and R. C. Mockler, IRE Trans. Instr. 9, 149 (1960).

BEL 53: E. H. Bellamy and K. F. Smith, Phil. Mag. 44, 33 (1953).

BOH 50: A. Bohr and V. Weisskopf, Phys. Rev. 77, 94 (1950).

BOH 53: A. Bohr and B. R. Mottelson, Kgl. Danske Videnskab. Selskab, Mat.-Fys. Medd. 27, 16 (1953).

BRA 60: N. Braslau, The Rubidium-85–Rubidium-86 Hyperfine Structure Anomaly (Ph. D. Thesis), Lawrence Radiation Laboratory Report UCRL-9130, March 21, 1960 (unpublished).

COH 57: E. R. Cohen, K. M. Crowe, and J. W. M. duMond, The Fundamental Constants of Physics (Interscience Publishers, Inc., New York, 1957).

EIS 58: J. Eisinger and V. Jaccarino, Rev. Mod. Phys. 30, Part I, 528 (1958).

EWB 61: W. B. Ewbank, private communication, 1961.

FER 33: E. Fermi and E. Segrè, Z. Phys. 82, 729 (1933).

HAH 56: B. Hahn, D. G. Ravenhall, and R. Hofstadter, Phys. Rev. 101, 1131 (1956).

KUS 49: P. Kusch and H. Taub, Phys. Rev. 75, 1477 (1949).

MAJ 32: E. Majorana, Nuovo Cimento 9, 43 (1932).

MIL 39: S. Millman, Phys. Rev. 55, 628 (1939).

NOY 58: H. Noya, A. Arima, and H. Horie, Prog. Theoret. Phys. (Kyoto) Suppl. 8, 33 (1958).

RAB 28: I. I. Rabi, S. Millman, P. Kusch, and J. R. Zacharias, Phys. Rev. 53, 318 (1938).

RAM 56: N. F. Ramsey, Molecular Beams (Clarendon Press, Oxford, 1956).

STR 57: H. H. Stroke, V. Jaccarino, D. S. Edmonds, and R. Weiss, Phys. Rev. 105, 590 (1957).

STR 61: H. H. Stroke, R. J. Blin-Stoyle, and V. Jaccarino, Phys. Rev. 123, 1326 (1961).

TOR 41: H. C. Torrey, Phys. Rev. 59, 293 (1941).

WAL 53: H. E. Walchli, Oak Ridge National Laboratory Report ORNL-1469, 1953 (unpublished).

YAF 49: L. Yaffe, M. Kirsch, S. Standil, and J. M. Grunlund, Phys. Rev. 75, 699 (1949).

ZUR 59: D. H. Zurlinden, private communication, 1959.